



**HAL**  
open science

# Image-based isogeometric twins of lattices with virtual image correlation for varying cross-section beams

Jean-Charles Passieux, Robin Bouclier, Oliver Weeger

## ► To cite this version:

Jean-Charles Passieux, Robin Bouclier, Oliver Weeger. Image-based isogeometric twins of lattices with virtual image correlation for varying cross-section beams. *International Journal for Numerical Methods in Engineering*, inPress, 24 p. 10.1002/nme.7208 . hal-03980174

**HAL Id: hal-03980174**

**<https://hal.science/hal-03980174>**

Submitted on 9 Feb 2023

**HAL** is a multi-disciplinary open access archive for the deposit and dissemination of scientific research documents, whether they are published or not. The documents may come from teaching and research institutions in France or abroad, or from public or private research centers.

L'archive ouverte pluridisciplinaire **HAL**, est destinée au dépôt et à la diffusion de documents scientifiques de niveau recherche, publiés ou non, émanant des établissements d'enseignement et de recherche français ou étrangers, des laboratoires publics ou privés.

## ARTICLE TYPE

# Image-based isogeometric twins of lattices with virtual image correlation for varying cross-section beams

Jean-Charles Passieux\*<sup>1</sup> | Robin Bouclier<sup>1,2</sup> | Oliver Weeger<sup>3</sup>

<sup>1</sup>Institut Clement Ader (ICA), Université de Toulouse, CNRS-INSA-UPS-ISAE-Mines Albi, Toulouse, France

<sup>2</sup>Institut de Mathématiques de Toulouse (IMT), Université de Toulouse, CNRS-INSA-UT1-UT2-UP, Toulouse, France

<sup>3</sup>Cyber-Physical Simulation, Department of Mechanical Engineering, Technical University of Darmstadt, Darmstadt, Germany

**Correspondence**

\*J.C. Passieux Email: passieux@insa-toulouse.fr

**Present Address**

135 avenue de Rangueil, 31077 Toulouse, Fr.

**Summary**

Cellular materials, in particular metal or polymer foams and beam lattices, are characterized by a complex architecture where the material is concentrated in slender struts. This study is concerned with the construction of numerically efficient sample-specific digital twin for the analysis and characterization of the mechanical behavior of such meta-materials. A method to build an explicit, light, and analysis-suitable isogeometric beam model directly from digital images is proposed. More precisely, as a main contribution, the Virtual Image Correlation method is extended to the case of multiple interconnected beams with varying cross-sections. Special care is also given to the initialization for better efficiency and robustness. Synthetic and real examples of increasing complexity, i.e. curved beams, lattices, and foams, are presented to account for the performance of the developed workflow from digital images to an isogeometric twin for mechanical modelling and simulation.

**KEYWORDS:**

image-based models, digital twin, isogeometric analysis, lattices, cellular materials

## 1 | INTRODUCTION

Cellular materials are currently gathering an important momentum in both the scientific and industrial communities<sup>1</sup>. They rely upon a simple idea: mimicking nature, such as bones and wood, which allows to achieve, in particular, unprecedented stiffness-to-weight ratios<sup>2</sup>. In practice, cellular materials are characterized by a complex micro-architecture. Most of times, the material is concentrated in small struts connected in different ways, at an intermediate scale between the constituents and the structure. Originally consisting of foams<sup>3,4</sup>, *i.e.* exhibiting a random distribution of cells, the advent of Additive Manufacturing (AM) now pushes these materials to a new stage: it becomes possible to produce so-called *lattices* where well-designed unit-cells are periodically (or quasi-periodically<sup>5</sup>) repeated all over a macro shape to obtain exceptional specific performances. Amongst others, lattices can be made highly stretchable<sup>6</sup>, auxetic<sup>7</sup>, and multi-functional, and therefore, besides being attractive for lightweight components, they appear of crucial interest for energy absorption, thermal management, design of medical implants, to name a few<sup>8,9,10,11</sup>.

However, due to the coexistence of two very different scales, the prediction of the mechanical behavior of such materials remains an issue, especially in non-linear regimes<sup>12,13,14,15</sup>. Their global response is actually intimately related to the local architecture, which may not be perfectly known *a priori*, either because of the random aspect in foams, or because of the strut-level process-induced defects and uncertainties in lattices<sup>16,17,18</sup>. In view of characterizing the mechanical behavior of such materials, it thus appears of paramount importance to build a digital mechanical twin for each individual tested sample<sup>19</sup>. This usually starts with performing X-ray micro-computed tomography ( $\mu$ -CT) to reveal the internal architecture of the cellular

material<sup>20</sup>. Then, the reconstructed volume images are used to build specimen-specific image-based models accounting for the real, as-manufactured geometric architecture of the structure<sup>21,22,12,23,24,18</sup>. The present work is heading in this direction: the objective is to develop a method to build light yet accurate image-based models of cellular materials, in particular, covering the situations of (open-cell) foams and beam lattices.

In this context, IsoGeometric Analysis (IGA), that employs the spline basis functions from Computer-Aided-Design (CAD) directly for the analysis<sup>25,26</sup>, seems to constitute an attractive path. Indeed, given the higher-order regularity of the spline functions, it may offer (i) a compact description of the geometry and (ii) an increased per-Degree-Of-Freedom (per-DOF) accuracy<sup>27</sup>, in comparison to the standard Finite Element Method (FEM). Nevertheless, classic image-based modeling techniques used in FEM (*e.g.*, the marching cube algorithm<sup>28,29</sup>) do not directly apply to IGA. In brief, the isogeometric image-based models proposed so far can be grouped in two main classes. On the one hand, *immersed methods* make use of a simple Cartesian spline mesh encompassing the scanned object, typically a box, for the discretization of the mechanical field. A voxel-based quadrature rule consistent with the topology of the architecture of interest is then defined, to include the constitutive behavior only in the area where there is material. Given their versatility with respect to the geometric complexity of the specimen, these methods have been applied in many fields, such as for the analysis of trabecular bones<sup>30,31</sup>, foams<sup>32,33</sup>, composite materials<sup>34,35</sup>, porous media<sup>36</sup> and AM lattices<sup>18,24</sup>. However, it is worth noting that (i) they only lead to an implicit representation of the geometry and (ii) their numerical complexity may be important, especially the numerical integration of cut elements remains challenging from an efficiency point of view<sup>37,38</sup>. On the other hand, *template-fitting methods* build a parameterized spline-based template geometry representative of the essential features of the specimen, and are accompanied by a control point fitting procedure to accurately match the scan data. Hence, these techniques require starting from a description whose topology is compatible with that of the scanned object but, in turn, they have the advantage of providing an explicit compact, IGA-suitable CAD description. Until now, this second class of methods seems to have been mainly applied in the biomedical field (see, *e.g.*,<sup>39,40,41</sup> for patient-specific blood-flow analyses in arteries, and<sup>42,43</sup> for mechanical and fluid-structure simulations of heart valves).

In our opinion, template-fitting methods also appear highly relevant in the case of cellular materials such as lattices, since the topology of the architecture is simply constituted by an assembly of beams. In this work, we thus undertake to apply the principle of template-fitting techniques to build an explicit B-spline based beam model, which is *analysis-suitable* in the sense that it is directly ready for isogeometric beam simulations. This results in a model which is extremely reduced in terms of numerical complexity. In case of lattices formed by repeating a given unit-cell, the topology may be known *a priori* from the CAD file. Yet, it is required to learn the beam topology from the images in case of foams, which is also addressed in this contribution by resorting to advanced image processing techniques<sup>44,45,46</sup>.

Now, the challenging task concerns the development of a dedicated fitting procedure that repositions the control points of the initial topology to properly fit the scan data. In order to do so, we propose to rely on the Virtual Image Correlation (VIC) method that has been specifically developed to measure a curve-type entity or a specimen boundary with a sub-pixel precision. Inspired from the global form of Digital Image Correlation (DIC)<sup>47,48,49,50</sup>, the principle is to create a virtual image representing the entity to be measured, and to look for the optimal position of the latter so that the virtual image best matches the real image in a small region surrounding the entity. Originally introduced by François *et al.*<sup>51,52</sup> to measure the curvature of bent beams or cables in digital images, the VIC approach has been improved over the years and its performance has been demonstrated for many applications. In this respect, one may mention, *e.g.*,<sup>53</sup> that introduces spline functions in VIC for better regularization and more efficiency,<sup>54</sup> where an explicit B-spline description of the entity to be measured is taken for the first time in VIC,<sup>55</sup> for a more recent extension in 3D to measure organ shapes in medical imaging,<sup>56</sup> for an attempt to complement DIC with VIC to reduce the measurement uncertainty near object boundaries, and<sup>57</sup> for an up-to-date analysis of the accuracy and robustness of the method.

In this work, the study is limited to the measurement of curve-type entities in 2D images. However, since our goal is to update a lattice-type geometry, we further consolidate the VIC technique by extending it (i) to the case of curved beams with varying cross-sections, and (ii) to the situation of multiple interconnected beams. In the literature of VIC for the measurement of beams, the thickness is so far never estimated and the considered beams/curves are of constant cross-section. Here, we therefore propose a new VIC algorithm that allows to finely measure the cross-section thickness in addition to the centerline position of beams. The key idea is to include the cross-section variation in the virtual image. Special care is also given to the initialization to minimize the layer width of the virtual image for better efficiency, and to the definition of the connectivity between the different beams for a simple handling of full lattices. Finally, the analysis-suitable feature of our beam image-based model is highlighted by carrying out mechanical simulations using the nonlinear isogeometric beam element developed in<sup>58,59,60</sup>.

The paper is organized as follows: Section 2 reviews the current VIC method for the measurement of the centerline of a single beam. Then, in Section 3, we present our extension of the VIC strategy to estimate the cross-section thickness in addition to the centerline, and we propose a procedure to simply define the connectivity of a full lattice. In Section 4, the mechanical model is built in a straightforward manner from the obtained geometric description, using an advanced isogeometric beam formulation that has proved to be relevant for the analysis of lattices. Finally, in Section 5, the performance of the developed beam image-based model is demonstrated through a series of examples involving synthetic and real images of beam lattices and foams, before concluding remarks are formulated in Section 6.

## 2 | STANDARD VIC FOR THE MEASUREMENT OF BEAM CENTERLINES

As outlined in the introduction, many versions of the Virtual Image Correlation (VIC) approach have been developed this last decade, varying in terms of optimization formulations and algorithms considered. We start here by focusing on the measurement of the centerline of a single beam. To do so, we choose to build the virtual image in the parameter space of spline functions and look for the spline mapping for which the virtual image fits, at best, the real image in a small region surrounding the sought spline beam centerline. The cost function is written in the parametric space, the virtual image size in the normal direction is fixed *a priori*, and a Gauss-Newton algorithm is used for the minimization. In this respect, the basics of our method are close to, *e.g.*,<sup>55,56</sup>.

### 2.1 | Formulation of the standard VIC problem

An overview of what we refer to as the standard VIC method is depicted in Fig. 1. In what follows, we specify the approach by elaborating on the theory behind this figure.

#### 2.1.1 | Virtual image

Here, we are interested in the measurement of a curve-type entity in the real image, denoted by  $f$ . It corresponds to a graylevel piecewise constant implicit description of a line, *e.g.* white-to-black-to-white variation of the graylevel within a narrow pixel band (see the background in Figs. 1(b) and 1(c)). As a consequence, we build the virtual image  $g$  in the parametric space  $(\xi, \eta)$  using a sinusoidal bell-shaped function along the  $\eta$ -direction:

$$g(\xi, \eta) = g_{bg} + \frac{1}{2}(g_{fg} - g_{bg}) \left( \cos\left(\frac{\pi\eta}{h}\right) + 1 \right), \quad \forall(\xi, \eta) \in [0, 1] \times [-h, h], \quad (1)$$

where  $g_{bg}$  and  $g_{fg}$  denote, respectively, the mean background (*e.g.* white) and foreground (*e.g.* black) graylevels. The virtual image is potted in Fig. 1(a). It mimics, in a smooth way, the real image in a region surrounding the beam. Let us notice that other functions could have been used for building the virtual image, such as linear or Gaussian distributions, but this choice of sinusoid appears to be a good compromise between simplicity and efficiency<sup>53</sup>. From here on, we also underline that  $\eta$  ranges from  $-h$  to  $h$  such that the mapping from the parametric to the physical space in the  $\eta$ -direction will be identity. In other words, the size of the virtual image in the direction normal to the contour (in pixels), referred to as *layer width* in the remainder of the paper, will be  $2h$  in the physical space (see below).

#### 2.1.2 | Spline beam mapping

Starting from a point  $(\xi, \eta)$  in the parametric space of the virtual image (see Fig. 1(a)), we then need to define the mapping  $\mathbf{x}(\xi, \eta)$  to the physical space, which will allow to match the real image in a region close to the sought beam centerline (see Fig. 1(c)) with the virtual image. Recalling that we seek for a geometry description similar to the one of isogeometric beams since our final goal is to build an isogeometric beam image-based model, we make use of the following mapping:

$$\mathbf{x}(\xi, \eta; \lambda_c) = \mathbf{x}_c(\xi; \lambda_c) + \eta \mathbf{n}_c(\xi; \lambda_c), \quad \forall(\xi, \eta) \in [0, 1] \times [-h, h], \quad (2)$$

where the beam centerline curve  $\mathbf{x}_c$  is discretized by means of spline functions and  $\mathbf{n}_c$  is the normal unit vector to the beam centerline. More precisely, we have:

$$\mathbf{x}_c(\xi; \lambda_c) = \sum_j N_j^c(\xi) \lambda_{c_j}, \quad (3)$$

where  $(N_j^c)_j$  are the (univariate) B-spline functions and  $(\lambda_{c_j})_j$ , gathered in  $\lambda_c$ , are the coordinates of the associated control points. The normal vector  $\mathbf{n}_c$  can then be simply computed as:

$$\mathbf{n}_c = \mathbf{e}_z \wedge \mathbf{t}_c \quad \text{with} \quad \mathbf{t}_c = \frac{\partial \mathbf{x}_c}{\partial \xi} \left\| \frac{\partial \mathbf{x}_c}{\partial \xi} \right\|^{-1}, \quad (4)$$

and where  $\mathbf{e}_z$  is the unit vector normal to the plane. Let us note at this stage that such a strategy is only suitable to measure a curved beam centerline. It does not give any insight on the possibly varying thickness of the beam.

### 2.1.3 | Image correlation cost function

Now that we have in hand the virtual image and the expression of the spline mapping from the parametric to the physical space, the idea is to find the control points  $\lambda_c$  that allow to match, at best, the virtual image (1) with the real one evaluated in the physical sub-region  $\mathbf{x}(\xi, \eta; \lambda_c)$ ,  $\forall (\xi, \eta) \in [0, 1] \times [-h, h]$  (see Fig. 1(c) again). As in DIC<sup>47,48</sup>, the considered metric is the  $L_2$ -norm of the graylevel residual. Let  $(\xi_i, \eta_i)_i$  be a uniform sampling of points in the parametric region  $[0, 1] \times [-h, h]$ , the optimization problem thus reads in the discrete setting:

$$\lambda_c = \arg \min_{\lambda_c^*} \sum_i \left( g(\xi_i, \eta_i) - f(\mathbf{x}(\xi_i, \eta_i; \lambda_c^*)) \right)^2. \quad (5)$$

The density of the sampling points is chosen two or three times larger than the density of the pixels in the physical subregion where  $f$  is evaluated<sup>51,54</sup> in order to mimic the spatial quadrature that results from the formation of a pixel. We emphasize here that the VIC problem is formulated in the parametric space of the spline mapping which will simplify the algorithm for the solution (see next section). The spline mapping is only used to evaluate the real image in a thin layer in the physical space. This also accounts for the low computational cost of such a VIC strategy. Besides, one can notice that, contrary to DIC, the cost function in (5) will not decrease, in general, towards values as low as the magnitude of the camera noise since the virtual and real images are different. However, as long as the virtual image is even in the  $\eta$ -direction, this has almost no effect on the accuracy thanks to the least square nature of minimization (5)<sup>51</sup>.

## 2.2 | Solution using a Gauss-Newton algorithm

### 2.2.1 | Algorithm

Problem (5) is an unconstrained non-linear least-squares problem. Hence, it is solved with a Gauss-Newton algorithm, which consists of replacing, at each iteration, the non-linear least-squares problem by an approximate, linear least-squares problem. This is achieved by linearizing the graylevel residual. Starting with initial guess  $\lambda_c^{(0)}$ , at iteration  $k + 1$ , an estimate  $\lambda_c^{(k)}$  being known, we look for  $\lambda_c^{(k+1)} = \lambda_c^{(k)} + \delta \lambda_c^{(k)}$  that minimizes the cost function in (5) where:

$$g(\xi_i, \eta_i) - f(\mathbf{x}(\xi_i, \eta_i; \lambda_c^{(k+1)})) \approx \underbrace{g(\xi_i, \eta_i) - f(\mathbf{x}(\xi_i, \eta_i; \lambda_c^{(k)}))}_{r_i^{(k)}} - \underbrace{\frac{\partial f}{\partial \mathbf{x}}(\mathbf{x}(\xi_i, \eta_i; \lambda_c^{(k)})) \frac{\partial \mathbf{x}}{\partial \lambda_c}(\xi_i, \eta_i; \lambda_c^{(k)})}_{\mathbf{J}_{f_i}^{(k)}} \delta \lambda_c, \quad \forall i. \quad (6)$$

In the above equation,  $\mathbf{J}_{f_i}^{(k)}$  and  $r_i^{(k)}$  correspond, at iteration  $k$  and at point  $(\xi_i, \eta_i)$ , to the Jacobian vector of the composed application  $f \circ \mathbf{x}$  with respect to  $\lambda_c$ , and to the graylevel residual, respectively. The Gauss-Newton algorithm thus results in solving, at each iteration, the following linear system:

$$\mathbf{H}_{VIC}^{(k)} \delta \lambda_c^{(k)} = \mathbf{b}_{VIC}^{(k)} \quad \text{with} \quad \begin{cases} \mathbf{H}_{VIC}^{(k)} = \sum_i \mathbf{J}_{f_i}^{(k)T} \mathbf{J}_{f_i}^{(k)} \\ \mathbf{b}_{VIC}^{(k)} = \sum_i \mathbf{J}_{f_i}^{(k)T} r_i^{(k)} \end{cases}. \quad (7)$$

Note that in practice the real image  $f$  is obviously interpolated and then derived so as to be able to evaluate both  $r_i^{(k)}$  and  $\mathbf{J}_{f_i}^{(k)}$ . This is performed in this work using a cubic spline scheme available in Python (library: `scipy.interpolate`<sup>61</sup>). It may also be noticed that  $\partial \mathbf{x} / \partial \lambda_c$  in (6) can be computed analytically given Eqs. (2), (3) and (4). In this work, we actually simplified  $\partial \mathbf{x} / \partial \lambda_c$  by considering that the variation of  $\mathbf{x}_c$  with respect to  $\lambda_c$  is more important than that of  $\mathbf{n}_c$ , which yields the following

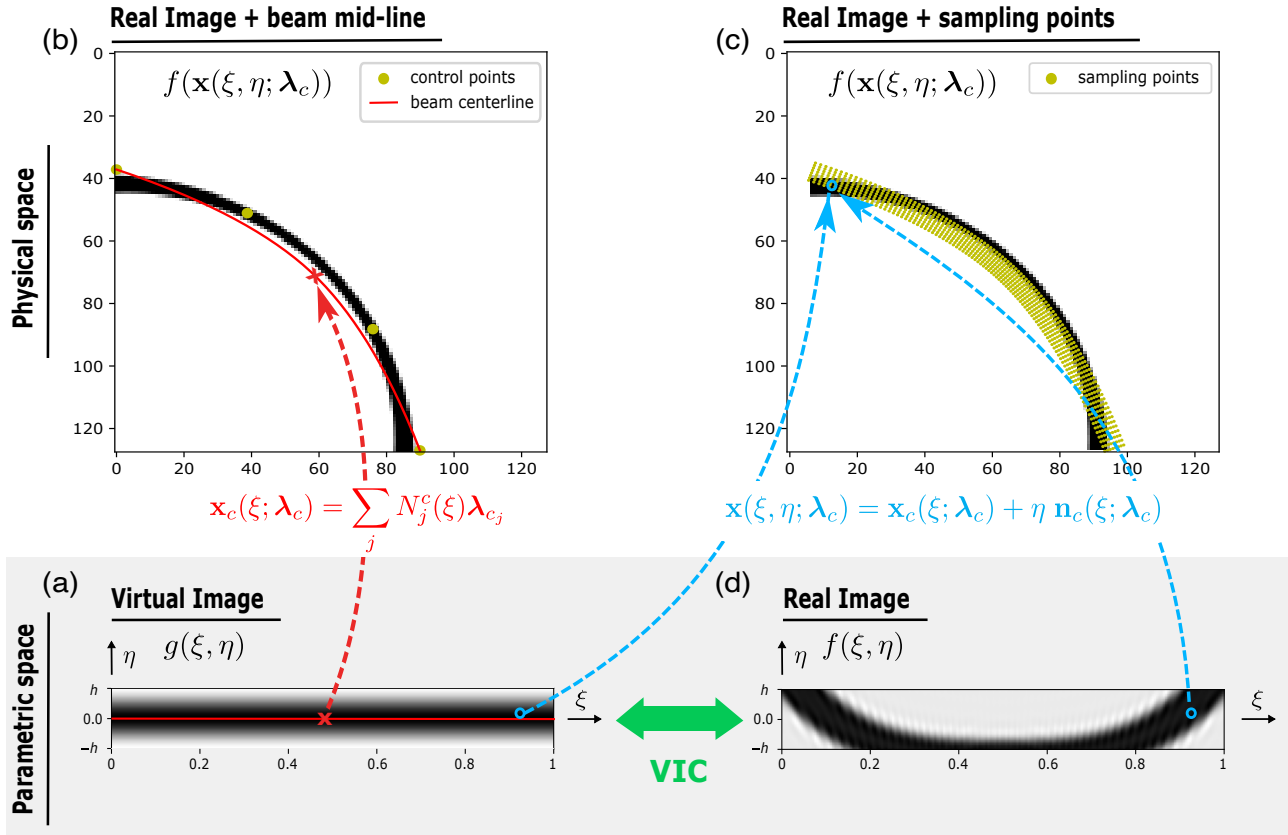


**FIGURE 1** Overview of the standard VIC method for the fitting of a beam centerline. (a) Virtual image  $g$  (see eq. (1)). (b) Real image (background) and a (not perfectly fitted) spline beam centerline along with its control points (foreground); the spline mapping for the beam centerline is indicated in red. (c) Real image (background) and sampling points used to evaluate the real image (foreground); the beam mapping that allows to map any sampling point from the parametric to the physical space is depicted in cyan. (d) Representation of the virtual image in the parametric space; the beam mapping is once again underlined in cyan. VIC consists of finding the location of the spline beam centerline that allows to best correlate the real image with the virtual one in the parametric space.

approximation:

$$\frac{\partial \mathbf{x}}{\partial \lambda_{c_j}} \approx \begin{bmatrix} N_j^c & 0 \\ 0 & N_j^c \end{bmatrix}, \quad \forall j. \quad (8)$$

We emphasize here that we do not need to compute the true Hessian matrix in algorithm (7) to achieve convergence. We only have to ensure that  $\delta \lambda_c^{(k)}$  constitutes a descent direction<sup>50</sup>, which has been the case in all the numerical experiments performed in this paper. Moreover, it has to be underlined that  $\lambda_c$  is voluntarily chosen of small dimension, *i.e.* that only few control variables are considered for the beam centerline, which helps regularizing the inverse problem (5). The last important ingredient concerns the initialization of the algorithm with  $\lambda_c^{(0)}$ . This point will be developed in next section.

To conclude, let us underline that, according to the literature, such a VIC method is able to measure a curve-type entity (or a specimen boundary) in a digital image with accuracy down to 1/1000 pixel<sup>51,52,53,57</sup>. The VIC variant reviewed in this section seems to be the most modern one<sup>55,56</sup>. It achieves a good compromise between simplicity and efficiency.

*Remark 1.* Contrary to DIC, it seems that no further assumption can be performed in theory to arrive at a constant Hessian matrix over all the iterations<sup>49,50</sup>. However, we emphasize again that the computational cost of VIC is low since only an univariate field is sought (*i.e.*, involving few DOF) and the problem is formulated over a thin region surrounding the beam to be measured (*i.e.*, involving few integration points).

### 3 | EXTENDING THE VIC METHOD TO BUILD IMAGE-BASED BEAM MODELS OF LATTICE STRUCTURES

As described above, classic VIC only provides access to the centerline. In this section, we propose a variant of the VIC algorithm so that it can measure the cross-section thickness in addition to the centerline position. The proposed algorithm can also estimate the cross-section thickness variations, since the latter are expected to vary along the beam centerline, especially on the boundaries (*i.e.*, the curve end-points, which are the attachment points with the other beams). Furthermore, we also propose a specific strategy for the initialization of the VIC algorithm that allows to minimize the layer width for better efficiency of the method. Finally, a specific pre-processing step is required to build the topology (*i.e.*, the organization and connection of the different beams) in case of a random beam lattice such as in more general cellular materials. For the presentation below, we first consider the case of a single beam with a varying thickness and then add a few remarks regarding the extension to the case of several, interconnected beams before the latter will be further illustrated in the examples section, see Section 5.

#### 3.1 | Taking into account a varying beam thickness

In order to measure the varying beam thickness in addition to the beam centerline, one may act either on the mapping (2) or on the virtual image (1). Although modifying the mapping (2) may be the most natural, it may complexify the solution stage since both the beam centerline and thickness variables will be involved in the real image term in the minimization (5). In particular, this would lead to the product of the beam centerline and thickness variables when performing the linearization (6). As a result, we rather include the beam thickness variables in the virtual image so that a classic Gauss-Newton algorithm can still be used for the minimization. For illustration purposes of the novel VIC method, the situation obtained at convergence with the same curved beam example as in Fig. 1 is depicted in Fig. 2. The method is detailed in the following.

##### 3.1.1 | Novel virtual image

We need to define a function that describes the smooth evolution of the beam thickness along  $\xi$  and include it in the sinusoidal bell-shaped distribution (1). Let us denote by  $t$  the beam thickness parameter, defined as a function of  $\xi$  since it may evolve along the center line. As for the centerline, we discretize  $t$  using B-spline functions; that is:

$$t(\xi; \lambda_t) = \sum_l N_l^t(\xi) \lambda_{t_l}, \quad (9)$$

where  $(N_l^t)_l$  are the B-spline functions and  $\lambda_t$  gathers all the (scalar) control parameters  $(\lambda_{t_l})_l$  of the thickness. With this in hand, we now propose to build the virtual image such as:

$$\bar{g}(\xi, \eta; \lambda_t) = \begin{cases} \text{if } |\eta| < t : & g_{bg} + \frac{1}{2}(g_{fg} - g_{bg}) \left( \cos \left( \frac{\pi \eta}{t(\xi; \lambda_t)} \right) + 1 \right) ; \\ \text{else :} & g_{bg} \end{cases} \quad \forall (\xi, \eta) \in [0, 1] \times [-h, h]. \quad (10)$$

A plot of this function is shown in Fig. 2(a). We observe that:

$$\left\{ \begin{array}{l} \bar{g} \left( \xi, \eta = \frac{t(\xi)}{2} \right) = \bar{g} \left( \xi, \eta = -\frac{t(\xi)}{2} \right) = \frac{g_{bg} + g_{fg}}{2} \\ \bar{g}(\xi, \eta = t(\xi)) = \bar{g}(\xi, \eta = -t(\xi)) = g_{bg} \\ \bar{g}(\xi, \eta = 0) = g_{fg} \end{array} \right. ; \quad \forall \xi \in [0, 1]. \quad (11)$$

Therefore, virtual image  $\bar{g}$  does mimic, in a smooth way, the real image in a region surrounding the beam. This ensures to obtain a relevant measurement for the centerline as well as for the thickness of the beam through a least-squares minimization similar to (5). In addition, we needed to propagate the signal for  $\eta \in [-h, -t(\xi)] \cup [t(\xi), h]$  to recover a rectangular image. This is naturally achieved by taking  $g_{bg}$  in this region, which also allows to maintain a  $C^1$  regularity at  $\eta = \pm t(\xi)$ . The so-called layer width  $2h$  (*i.e.* the virtual image size in the normal direction) is fixed and should not be confused with the real beam cross-section thickness parameter  $t$ . Obviously, the fixed layer width  $2h$  needs to be taken at least twice larger than the maximal thickness of

the beam. With the strategy we propose for the initialisation of VIC, we will see that we can actually take exactly twice the size of the maximal thickness without altering the robustness of the algorithm (see Sections 3.3 and 5.1).

Once again, we emphasize that we do not modify the mapping (2). In particular, it is still identity in the  $\eta$ -direction so that the obtained thickness  $t$  in the virtual image will also be the true thickness of the beam in the physical space (see Fig. 2(b)).

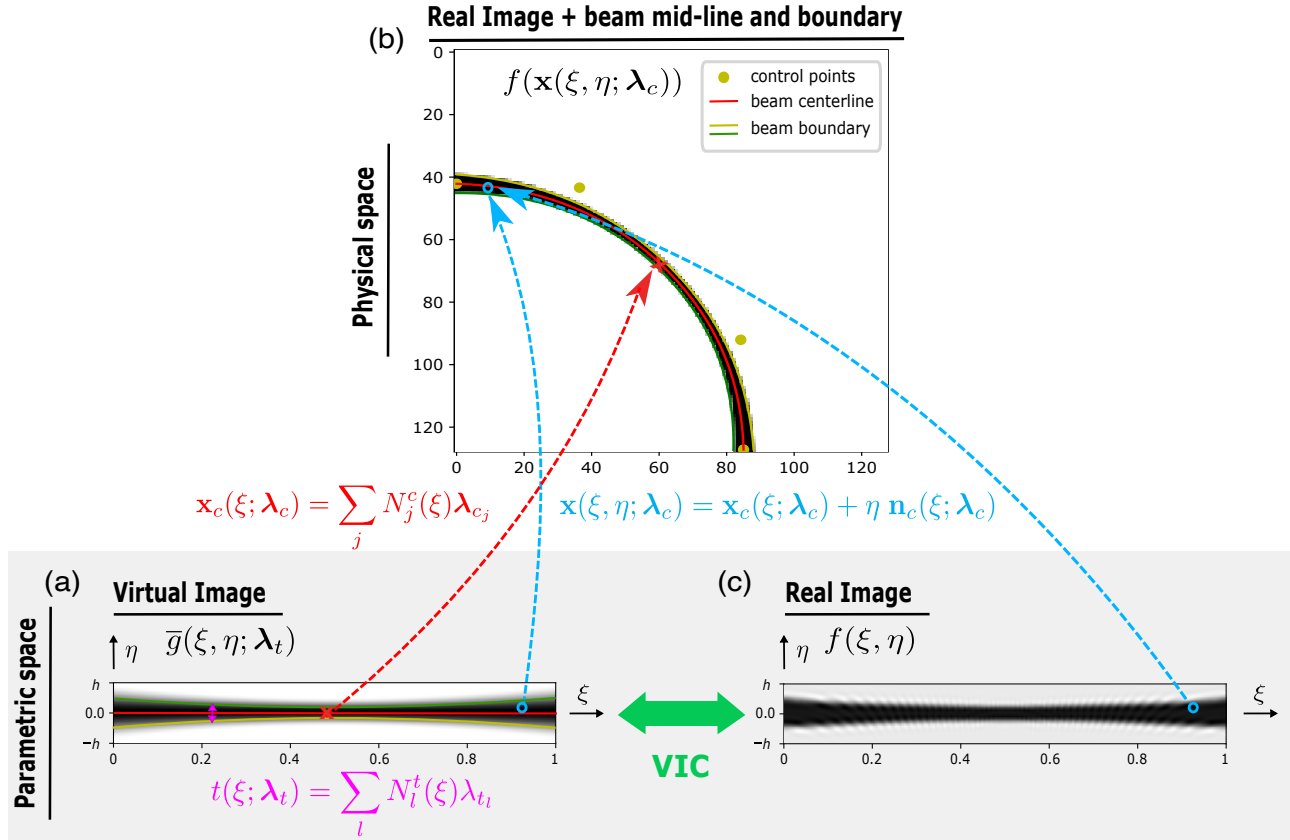


**FIGURE 2** Novel VIC method for the fitting of a beam centerline along with its varying thickness. (a) Virtual image  $\bar{g}$  (see eq. (10)) that incorporates the varying beam thickness  $t$  (see formula in magenta). (b) Real image (background) and spline beam centerline along with its control points and the beam boundary (foreground); the spline mapping for the beam centerline is indicated in red while the beam boundary is colored in yellow and green. (c) Representation of the virtual image in the parametric space; the beam mapping that allows to map any sampling point from the parametric to the physical space is depicted in cyan. The novel VIC method consists of finding the location of the spline beam centerline along with the distribution of the graylevel along the thickness direction  $\eta$  in the virtual image that allows to best correlate the real image with the virtual one in the parametric space.

### 3.1.2 | Formulation and solution for the extended VIC

Starting with (5), the extended minimization problem to be solved is straightforward: we look for both the beam centerline and thickness control parameters  $\lambda_c$  and  $\lambda_t$ , respectively, such that:

$$\lambda_c, \lambda_t = \arg \min_{\lambda_c^*, \lambda_t^*} \sum_i \left( \bar{g}(\xi_i, \eta_i; \lambda_t^*) - f(\mathbf{x}(\xi_i, \eta_i; \lambda_c^*)) \right)^2. \quad (12)$$



Then, in view of performing again a Gauss-Newton algorithm, we linearize the residual at each iteration. Recycling the notations of Section 2, this yields for iteration  $k + 1$ :

$$\bar{g}(\xi_i, \eta_i; \lambda_t^{(k+1)}) - f(\mathbf{x}(\xi_i, \eta_i; \lambda_c^{(k+1)})) \approx r_i^{(k)} + \underbrace{\frac{\partial \bar{g}}{\partial \lambda_t}(\xi_i, \eta_i; \lambda_t^{(k)})}_{\mathbf{J}_{\bar{g}_i}^{(k)}} \delta \lambda_t - \mathbf{J}_{f_i}^{(k)} \delta \lambda_c, \quad \forall i, \quad (13)$$

where  $\mathbf{J}_{\bar{g}_i}^{(k)}$  denotes, at iteration  $k$  and at point  $(\xi_i, \eta_i)$ , the Jacobian vector of  $\bar{g}$  with respect to  $\lambda_t$ . Once again, the latter can be computed analytically. It simply reads:

$$\frac{\partial \bar{g}}{\partial \lambda_t} = N_l \frac{\partial \bar{g}}{\partial t}, \quad \forall l. \quad (14)$$

Eventually, reporting approximation (13) in (12) leads to solving the following augmented linear system to get the Gauss-Newton update at iteration  $k + 1$ :

$$\begin{bmatrix} \mathbf{H}_{VIC}^{(k)} & -\mathbf{H}_{VG}^{(k)} \\ -\mathbf{H}_{VG}^{(k)T} & \mathbf{H}_G^{(k)} \end{bmatrix} \begin{bmatrix} \delta \lambda_c^{(k)} \\ \delta \lambda_t^{(k)} \end{bmatrix} = \begin{bmatrix} \mathbf{b}_{VIC}^{(k)} \\ \mathbf{b}_G^{(k)} \end{bmatrix}, \quad (15)$$

with:

$$\begin{cases} \mathbf{H}_{VG}^{(k)} = \sum_i \mathbf{J}_{\bar{g}_i}^{(k)T} \mathbf{J}_{f_i}^{(k)} \\ \mathbf{H}_G^{(k)} = \sum_i \mathbf{J}_{\bar{g}_i}^{(k)T} \mathbf{J}_{\bar{g}_i}^{(k)} \end{cases} \quad \text{and} \quad \mathbf{b}_G^{(k)} = \sum_i -\mathbf{J}_{\bar{g}_i}^{(k)T} r_i^{(k)}. \quad (16)$$

Making use once again of only a few control variables for the beam centerline and beam thickness helps regularizing problem (12). The computational cost is obviously more expensive since the system includes additional DOFs describing the beam thickness variation. However, the overall computational cost is still very limited since it only requires the additional computation of  $\mathbf{J}_{\bar{g}_i}^{(k)}$ , which is immediate.

*Remark 2.* There are situations (*i.e.* constant thickness) in which, provided that the synthetic and real images are symmetric with respect to the centerline, the VIC method is said to converge to the correct solution even if the thickness in the virtual image does not exactly match the real thickness<sup>51</sup>. In such situations, system (15) is not coupled and can be solved sequentially: first standard VIC (only centerline), then thickness determination by solving:

$$\mathbf{H}_G^{(k)} \delta \lambda_t^{(k)} = \mathbf{b}_G^{(k)}. \quad (17)$$

However, we will see in the examples section that in the general case, this system is coupled, *i.e.* there is a bias on the position of the centerline if the right thickness is not used for  $g$  (see Section 5.1 and Fig. 5). Searching for the thickness along with the centerline position is also the key element to consider interconnecting beams and to describe precisely the position of connecting nodes.

*Remark 3.* Furthermore, let us mention that the standard VIC problem (7) may be ill-conditioned. Updating the position of the centerline by moving the control points only in specific directions (such as along the normal to the centerline) can be a solution but it drastically reduces the design space. In this context, we noticed that considering in addition the thickness variation and formulating the coupled problem (15) with the same spline parameterization and same control parameters for the centerline (see Eq. (3)) and thickness (see Eq. (9)) regularized a lot the problem since the control parameters allow to better describe both the centerline the cross-section evolution. Note finally that in some situations the problem may still require an extra regularization of the centerline control point positions along the tangent direction, for example a Tikhonov-like regularization based on elasticity as performed in DIC<sup>62,33</sup>, to convexify it and help choosing a particular solution.

### 3.2 | Thickness estimation from thickness parameter

The real value of the beam cross-section thickness  $t_r$  is not necessarily equal to what we referred to as thickness parameter  $t$  in Eq. (9). The estimation of the thickness of the beams requires a post-processing phase that is detailed in this subsection from the theoretical analysis of a simple one-dimensional example.

Let us consider a synthetic real image  $f(\eta)$  equal to  $f_{fg} = 1$  for all  $\eta$  such that  $|\eta| < t_r/2$  with a real thickness of  $t_r = 1$  and  $f_{bg} = 0$  otherwise. Only a half of the beam (in the  $\eta$ -direction) is considered since both  $f$  and  $g$  are even with respect to the

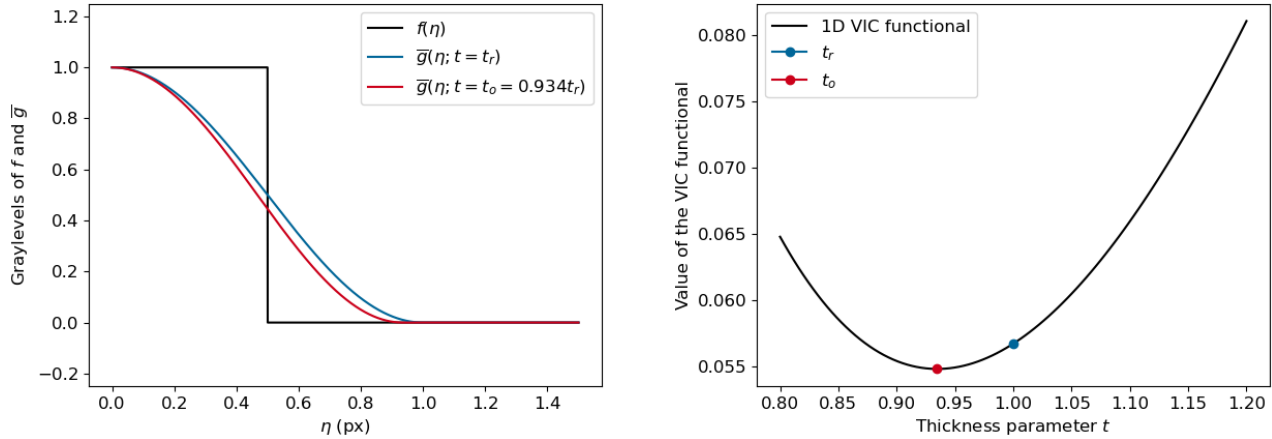


**FIGURE 3** Illustration of the 1D analytical problem to estimate the real thickness of the beam. Left: the virtual images  $\bar{g}$  for two characteristic values of the thickness parameter  $t$  are compared to the real image  $f$ . Right: the evolution of the VIC functional and localisation of the same characteristic values of  $t$ .

centerline that is considered fixed here. Let  $\bar{g}(\eta; t)$  be the virtual image where  $t$  is the thickness parameter. It is build from (10) with  $g_{bg} = 0$  and  $g_{fg} = 1$ . The optimal thickness parameter  $t_o$  minimises the VIC functional (12):

$$t_o = \arg \min_t \int_{\eta=0}^t (\bar{g}(\eta; t) - f(\eta))^2 d\eta. \quad (18)$$

As mentioned above,  $t_o$  does not correspond to  $t_r$ . In the following, we show how to estimate the real thickness  $t_r$  of the beam from the optimal  $t_o$  (optimal in the sense of (3.2)). Considering the particular shape of  $f$  and  $\bar{g}$ , the functional (3.2) becomes:

$$\int_{\eta=0}^t (\bar{g}(\eta; t) - f(\eta))^2 d\eta = \frac{1}{4} \int_0^{t_r} \left(1 - \cos\left(\frac{\pi\eta}{t}\right)\right)^2 d\eta + \frac{1}{4} \int_{t_r}^t \left(1 + \cos\left(\frac{\pi\eta}{t}\right)\right)^2 d\eta = \frac{3}{4}t - \frac{t}{\pi} \sin\left(\pi \frac{t_r}{t}\right). \quad (19)$$

The stationary condition of functional (19) with respect to  $t$  reads:

$$\frac{3}{4} + \frac{t_r}{t_o} \cos\left(\pi \frac{t_r}{t_o}\right) - \frac{1}{\pi} \sin\left(\pi \frac{t_r}{t_o}\right) = 0. \quad (20)$$

By solving non-linear equation (20), it comes that the ratio between the optimal  $t_o$  and the actual  $t_r$  values of the thickness is such that  $t_o/t_r = 0.93467927$ . This result provides a simple way to estimate *a posteriori* the true thickness  $t_r$  of each beam from the optimal value  $t_o$ . Since it is a simple linear scaling, it is sufficient to scale the value of the control parameters  $\lambda_i$ .

An illustration is given in Fig. 3. More precisely, Fig. 3 (left) plots half of the virtual and real images as a function of  $\eta$  for two characteristic values of the virtual thickness parameter  $t$ . The evolution of the functional is given in Fig. 3 (right) and the value of the functional is given for the same two characteristic values of  $t$ . This figure numerically confirms that the optimal value  $t_o$  of  $t$  is not equal to the real image thickness  $t_r$ , and it confirms also the value of the scaling parameter.

In the remainder of the article and especially in the examples section, even if not specified, when we mention or display the *thickness*, it refers to  $t_r$ .

*Remark 4.* We call this an estimation because this scaling may be approximate especially in the case where the actual graylevel distribution in the real image  $f$  does not follow exactly a square window or if the values of  $f_{bg}$ ,  $f_{fg}$  are corrupted with noise. Anyway, it is shown in the example section that the estimation of the thickness leads to very accurate mechanical models. There might probably be other virtual images that could be less (or not at all) sensitive to this issue. Regularized square windows or spline descriptions of the graylevels could be considered. A regular virtual image with a sharp gradient and, most importantly, whose gradient does not depend on the thickness parameter, could improve the method.

### 3.3 | Initialization of the VIC algorithm

Since it is based on a Newton-type algorithm, the proper initialization of the VIC algorithm is necessary to make it converge. For the present case of beams, it seems that the initial positions of the centerline control points along with the layer width  $2h$  must be chosen such that the sampling region (see the yellow dots in Fig. 1(c)) covers entirely the *white-to-black-to-white* variation of the graylevel in the real image<sup>51</sup>. This requires either to initialize the positions of the centerline control points very close to the solution or to take a sufficiently large layer width  $2h$  for the virtual image. The first solution is not always an easy task, while the second one may substantially increase the computational cost of the method.

As a remedy, we propose here to run in a pre-processing step minimization (5) with  $g = g_{fg}$ ,  $\forall(\xi, \eta) \in [0, 1] \times [-h, h]$ . This is very simple from algorithm (7) and allows to position, in very few iterations, the centerline control points such that the region of the sampling points embeds the real beam. The layer width  $2h$  can thus be taken as the minimal possible, *i.e.* twice larger than the maximal thickness of the beam. Only a non-empty intersection of the region of the sampling points with the real beam centerline is required to make this initialization algorithm converge. Note that this treatment seems to constitute an additional contribution of this work to the field of VIC and, as a consequence, will be further accounted for in the examples section (see especially Section 5.1).

*Remark 5.* Once the algorithm is initialized, we can also benefit from the attractive refinement capabilities of B-splines to solve the optimization problem (12) in a multilevel fashion (as performed, *e.g.*, for shape optimization<sup>63,64</sup> or in the field of DIC<sup>65,66</sup>). It consists in first running algorithm (15) using coarse splines spaces for  $\lambda_c$  and  $\lambda_t$ , and then refining the spline spaces (usually by knot-insertion) and running again algorithm (15) while starting with the solution obtained after the previous optimization. This will be performed in the numerical results section, see Subsections 5.2 and 5.3.

### 3.4 | Consideration of interconnected beams

The extension of the new VIC approach to foams or lattice-type structures made of several interconnected beams requires the proper definition of the connectivity of the lattice. By connectivity here we mean that we need to associate, for each beam, the control points and the control parameters that describe, respectively, the centerline and thickness variation of the considered beam.

More precisely, we propose to proceed as follows for the definition of the connectivity. First, the beam lattice topology, *i.e.* the delimitation of the different beams, is defined such that the beams connect only on their ends. Then, each beam centerline is discretized using an open knot-vector (see, *e.g.*,<sup>67,68</sup>), which implies that the first and last control points are interpolatory at the ends of the centerline. In addition, we make sure to take a single end control point when several beams are adjacent to a certain node of the structure. Finally, we perform similarly for the thickness variation of each beam (open knot-vectors and same thickness at the beams ends when the beams are adjacent at that location). For illustration purpose, we refer to Fig. 9(b) (the latter being detailed in the example section). This treatment makes the implementation of VIC for a full lattice straightforward; indeed, a standard FE assembly procedure can be used to aggregate the beam-wise system (15) into one large system associated to the whole structure.

From the steps outlined above, the crucial one concerns the construction of the beam lattice topology. In case of a lattice structure formed by repeating a given beam-type pattern, such as a unit-cell obtained by AM, the lattice topology may be known *a priori* from the CAD file. However, this is not the case for more general cellular materials such as open-cell foams. In these situations, the beam topology needs to be built from the images. In order to do so, it may be necessary to resort to advanced methods from the image processing field, such as skeletonization<sup>44</sup>, level-set<sup>45</sup>, and watershed methods<sup>46</sup>. In particular, we managed to build the topology of a 2D structure mimicking the microstructure of an open-cell foam with such methods. The procedure is specified in the examples section (see especially Section 5.3).

## 4 | MECHANICAL ANALYSIS OF THE CONSTRUCTED IMAGE-BASED BEAM LATTICE MODELS

The last step to achieve image-based modeling is to simulate the mechanical behavior of the obtained beam lattice geometry. With the model built in the previous section, this process is seamless since the latter uses a spline-based geometric description that is exactly the one encountered in isogeometric methods for beams. Thus, we only provide a brief review of the considered

isogeometric beam element here, which is the one introduced in<sup>58</sup>. It now appears highly relevant for the analysis of lattice structures given, in particular, its ability to incorporate spatially varying geometric parameters such as the beam thickness<sup>59,60</sup> and its extension to inelastic regimes<sup>69</sup>. Only the fundamentals are outlined in the following. For simplicity, we restrict ourselves to 2D and elasticity (but possibly with large deformations and rotations). For further details, the reader is referred to the works cited herein.

#### 4.1 | Mechanical boundary value problem

Starting with the initial geometry of the 2-dimensional beam continuum  $\mathbf{x}$  defined under the form (2), *i.e.* in terms of its centerline curve  $\mathbf{x}_c$  and normal vector  $\mathbf{n}_c$ , as well as its thickness curve  $t$ , see (9), the aim now is to compute the deformed configuration of the structure when subjected to a certain loading and boundary conditions.

To derive the beam formulation, it may first be needed to introduce the arc-length parameterization of the beam. It consists of using, instead of  $\xi$  in previous sections, the curvilinear abscissa  $s \in [0, L]$ , where  $L$  is the length of the beam. Obviously,  $s$  can be computed from  $\xi$  as:

$$s = \phi(\xi) = \int_{\xi_0=0}^{\xi_0=\xi} \left\| \frac{\partial \mathbf{x}_c}{\partial \xi} \right\| d\xi_0. \quad (21)$$

With (21), it is possible to express the beam quantities in terms of  $s$  instead of  $\xi$ . For instance, this means that we can now express the arc-length parameterized beam centerline  $\mathbf{x}_c^s$  such that:

$$\mathbf{x}_c^s : [0, L] \rightarrow \mathbb{R}^2 ; \phi(\xi) \rightarrow \mathbf{x}_c(\xi), \quad (22)$$

with  $\mathbf{x}_c(\xi)$  from (3). Thus, in the arc-length parameterization, the tangent of the centerline curve always has unit length:

$$\|\mathbf{x}_c^{s'}\| = \left\| \frac{\partial \mathbf{x}_c^s}{\partial s} \right\| = 1, \quad \forall s \in [0, L]. \quad (23)$$

In the following, we consider that all the beam quantities are expressed in terms of  $s$  and the arc-length derivative  $' = \partial/\partial s$ . However, for the sake of readability, we omit the superscript  $s$ .

The deformed configuration  $\mathbf{x}^*$  of the beam can then be described as:

$$\mathbf{x}^*(s, \eta) = \mathbf{x}_c(s) + \mathbf{u}_c(s) + \eta \mathbf{R}(\theta_c(s)) \mathbf{n}_c(s), \quad \forall (s, \eta) \in [0, L] \times [-t(s)/2, t(s)/2], \quad (24)$$

where  $\mathbf{u}_c(s)$  is the displacement of the centerline curve and  $\theta_c(s)$  the rotation angle of the current cross-section w.r.t. the initial normal  $\mathbf{n}_c$ ,  $\mathbf{R}(\theta) = \begin{pmatrix} \cos \theta & -\sin \theta \\ \sin \theta & \cos \theta \end{pmatrix}$  being a 2D rotation matrix.

The initial and current directors of the beam  $\mathbf{A}_i$  and  $\mathbf{a}_i$ , respectively, are defined as:

$$\mathbf{A}_1(s) = \mathbf{x}'_c = \mathbf{t}_c \quad (\text{see also (4)}), \quad \mathbf{A}_2(s) = \mathbf{n}_c, \quad \mathbf{a}_1(s) = \mathbf{t}_c + \mathbf{u}'_c, \quad \mathbf{a}_2(s) = \mathbf{R}(\theta) \mathbf{n}_c. \quad (25)$$

Then, following the Timoshenko beam theory, the kinematics of the potentially initially curved, shear-deformable 2D beam are defined in terms of the axial (tensile), shear, and curvature strains<sup>70</sup>:

$$\varepsilon(s) = \frac{1}{2} (\mathbf{a}_1 \cdot \mathbf{a}_1 - \mathbf{A}_1 \cdot \mathbf{A}_1), \quad \gamma(s) = \mathbf{a}_1 \cdot \mathbf{a}_2, \quad \kappa(s) = \mathbf{a}_1 \cdot \mathbf{a}'_2 - \mathbf{A}_1 \cdot \mathbf{A}'_2. \quad (26)$$

Assuming a linear elastic material behavior, from these strain measures, the axial and shear forces as well as the bending moment are calculated by integrating the stresses over the beam cross-section, resulting in:

$$n(s) = EA \varepsilon, \quad q(s) = GA \gamma, \quad m(s) = EI \kappa. \quad (27)$$

Here,  $E$  is the Young's modulus and  $G$  the shear modulus of the material, and  $A$  and  $I$  are, respectively, the area and second moment of area of the cross-section. For instance, one has  $A = \pi (t/2)^2$  and  $I = \pi/4 (t/2)^4$  for a circular and homogeneous cross-section, or  $A = bt$  and  $I = bt^3/12$  for a rectangular cross-section of width  $b$ . Note that  $A$  and  $I$  depend also on  $s$  through the varying thickness  $t(s)$ .

Now, the balance equations of linear and angular momentum can be expressed for  $s \in (0, L)$  as:

$$n' + \bar{n} = 0, \quad q' + \bar{q} = 0, \quad m' - \mathbf{a}_1 \cdot \begin{pmatrix} q \\ n \end{pmatrix} + \bar{m} = 0, \quad (28)$$

where  $\bar{n}$ ,  $\bar{q}$ , and  $\bar{m}$  are external axial tensile and shear force, and bending moments, respectively. Given suitable boundary conditions for the displacements and rotations or forces and moments at the beam ends  $s = 0$  and  $s = L$ , the boundary value problem (BVP) for the nonlinear equations (28) uniquely determines  $\mathbf{u}_c$  and  $\theta_c$ .

## 4.2 | Numerical solution using isogeometric collocation

Since it is generally not possible to solve the BVP of (28) analytically, we apply here a numerical discretization using an isogeometric collocation method<sup>71,72</sup>. First, the displacement field  $\mathbf{u}_c$  and rotation angle field  $\theta_c$  are also discretized using B-spline functions:

$$\mathbf{u}_c(s, \lambda_u) = \sum_k N_k^u \circ \phi^{-1}(s) \lambda_{u_k}, \quad \theta_c(s, \lambda_\theta) = \sum_k N_k^\theta \circ \phi^{-1}(s) \lambda_{\theta_k}, \quad (29)$$

where  $N_k^u$  are typically a  $k$ -refined version<sup>73</sup> of the B-spline functions used to describe  $\mathbf{x}_c$  in (3), and  $\lambda_u$  and  $\lambda_\theta$  are the sets of control variables associated with  $\mathbf{u}_c$  and  $\theta_c$ , respectively. Then, the strong form of the BVP given by (28) is collocated at evaluation points  $\hat{s}_k \in (0, L)$ :

$$n'(\hat{s}_k) + \bar{n}(\hat{s}_k) = 0, \quad q'(\hat{s}_k) + \bar{q}(\hat{s}_k) = 0, \quad m'(\hat{s}_k) - \mathbf{a}_1(\hat{s}_k) \cdot \begin{pmatrix} q(\hat{s}_k) \\ n(\hat{s}_k) \end{pmatrix} + \bar{m}(\hat{s}_k) = 0. \quad (30)$$

By choosing the points  $\hat{s}_k = \phi(\hat{\xi}_k)$ , with  $\hat{\xi}_k$  being the Greville abscissae of the knot vector that defines  $N_k^u$ , and adding the boundary conditions, the number of collocation points is equal to the number of unknowns and one obtains a well-posed nonlinear system of algebraic equations that uniquely defines  $\lambda_u$  and  $\lambda_\theta$ . Here, this system is solved by a Newton-Raphson method, for which the derivatives can be analytically computed.

For lattice structures (*i.e.*, assemblies composed of several beams), the discretized and collocated equations given by (30) are aggregated into one big system and for all beams adjacent to a certain node of the structure the boundary conditions are replaced with coupling conditions that enforce the continuity of both  $\mathbf{u}_c$  and  $\theta_c$ .

For the numerical results presented in this work, in fact an equivalent 3D beam theory and isogeometric collocation method are used, which are described in detail in<sup>58</sup>, including the coupling conditions for beam structures and a mixed method that avoids shear locking effects.

## 5 | EXAMPLES

To assess the performance of the developed image-based beam model, we now investigate three 2D examples of increasing complexity both in terms of image data and geometries. In the first two examples the images are synthetically built, while in the third one the analysis of a real image is performed. The first example (Section 5.1) concerns a single curved beam with both constant and varying thickness, for which the exact geometry is known. The second example (Section 5.2) considers a network of beams, more precisely an auxetic lattice meta-material, to be constructed from a unit cell determined by topology optimization. The last example (Section 5.3) presents a complex random network of beams representative of an open-cell foam and thus, in addition to validating the method over a real image, illustrates the automatic construction of an initial beam model compatible with the topology of the sample. For the last two examples, mechanical simulations are performed using the isogeometric beam element introduced above in Section 4 and also compared to 2D FEM to demonstrate the analysis-suitable property and mechanical twin capability of our image-based model. Let us recall that, in all the examples, *thickness* refers to the real beam cross-section thickness  $t_r$ , and not the thickness parameter  $t$ .

### 5.1 | Synthetic curved beam

For this first very simple example, the synthetic image of the curved beam already used in Figs. 1 and 2 is studied. The centerline of the beam is a quarter circle and its cross-section varies quadratically with the angle, ranging between 2.8 (at  $\pi/4$ ) and 6.4 (at  $0$  and  $\pi/2$ ) pixels approximately. The synthetic image was created from a binary 8-bit image of  $2048 \times 2048$  pixel<sup>2</sup>, then the graylevels were obtained by binning to reach a definition of  $128 \times 128$  pixel<sup>2</sup>. This example allows us to quantify the error on the centerline for a proper comparison of the standard VIC (classic VIC with constant thickness as described in Section 2) and the new VIC approach (the proposed extension of VIC to varying and interconnected beams of Section 3). In addition, it highlights

the performance of the initialization technique proposed in Section 3.3. The results are grouped in Fig. 4 and additional plots regarding the error are realized in Figs. 5 and 6.

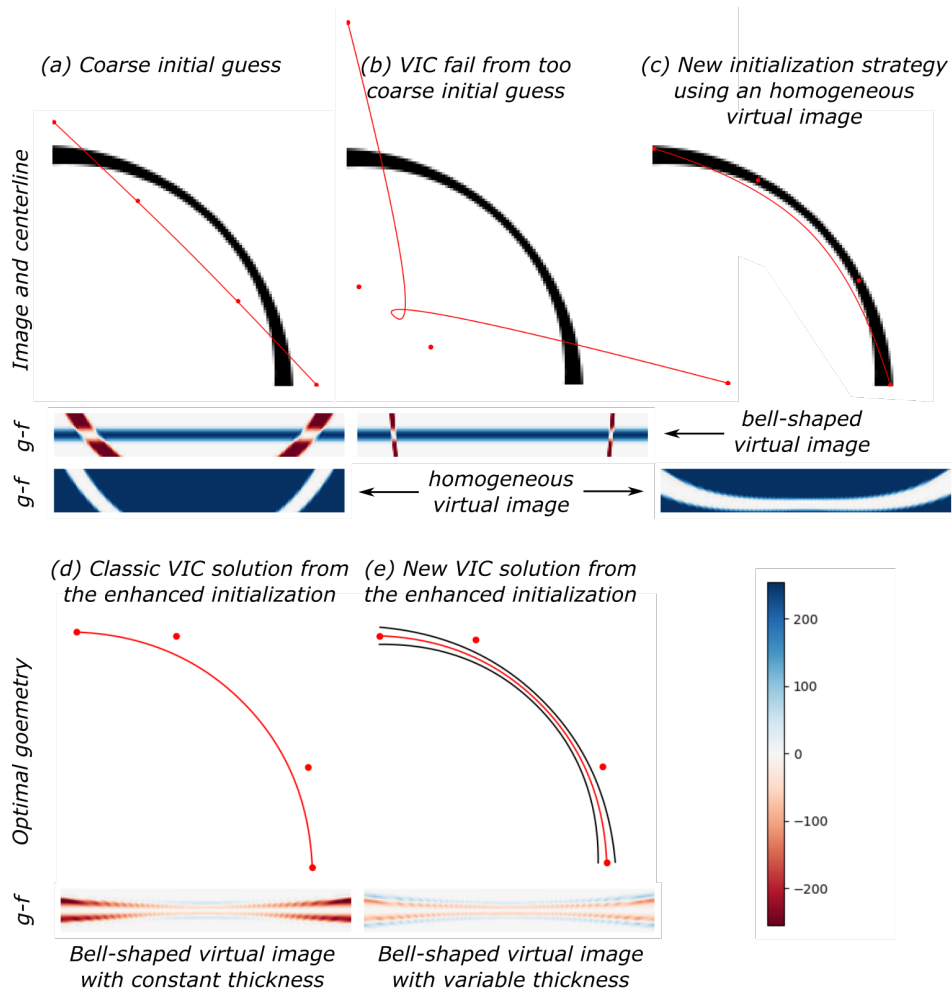


**FIGURE 4** Example of a synthetic image of a single beam with varying thickness. Initialization using a homogeneous virtual image and comparisons between the standard and proposed VIC variants.

### Initialization

We started with an initialization far enough from the solution, see Fig. 4(a). The initial model was simply a straight line made by a degree 2 B-spline curve with 4 regularly spaced control points. The first and last control points were forced to remain on the edges of the image, such that the total number of DOF was 6 for the centerline, with possible 4 additional DOF for the thickness in the proposed version of the VIC.

Fig. 4(a) also presents the residual  $g - f$  in the parametric space with a diverging colormap, such that the real image  $f$  appears in red, the virtual one  $g$  in blue, and it becomes white when the graylevels of  $f$  and  $g$  correspond to each other. Note that, in this section,  $g$  denotes indifferently the virtual image for the classic or new VIC method.

Starting from this initial guess, both classic and new VIC procedures did not converge when the standard bell-shaped virtual image was used, see Fig. 4(b). Indeed, as explained in Section 3.3, the sampling region must cover entirely the beam in the real image  $f$ , which was not the case with this initial guess. Instead of increasing the layer width  $2h$  (and therefore the computational cost), we considered the proposed alternative based on a homogeneous virtual image  $g$ . The corresponding residual map is given in Fig. 4(a) at the very bottom. To reduce the value of this residual, the same classic VIC algorithm was used. It actually aimed at maximizing the white area, which made the control points (and therefore the sampling area) move so that it completely covered

the beam in the real image. Figure 4(c) presents the solution of this technique and the corresponding residual after convergence. Once all the beam was in the sampling region, the algorithm stagnated. The corresponding solution was next used to initialize the classic and new VIC methods.

### Analysis of the VIC results

Starting from this enhanced initialization, see Fig. 4(c), and considering a bell-shaped virtual image with constant thickness equal to 4 pixels, the standard VIC algorithm converged to the solution depicted in Fig. 4(d). As explained in the literature, the VIC method adequately estimates the position of the centerline even though the thickness is not accurate. This results in the fact that the residual map does not vanish completely. The fact that both real and virtual images are even is sufficient to determine the centerline accurately. Finally, the proposed version of VIC with varying thickness was run on this example from the same enhanced initialization. Figure 4(e) presents the results. The centerline is almost the same as for the classic VIC, but it can be seen that the new algorithm provides, in addition, an explicit representation of the evolution the thickness along the centerline (yellow lines). The residual map does not have to tend towards 0 either, but it can be noticed that the level of residuals is far lower compared to the standard VIC, which means that the virtual image reproduces the real image better and therefore that we achieved a better knowledge of it.

### Robustness to initial thickness of the virtual image

Finally, the robustness of both VIC algorithms to the initial thickness is studied. To do so, we repeat the procedure previously performed (that is: first, enhanced initialization; then, VIC algorithm) for different initial values of the thickness  $t_v$ . For each run, the distance from the center of the circle to each point of the center line is computed. Then the standard deviation of its distribution is computed to estimate the circularity error in pixels. Figure 5 presents the evolution of this indicator as a function of the initial thickness for the standard and proposed VIC and for a synthetic image with a constant thickness and a varying thickness. It appears that, in the case of a curved beam of varying thickness, the initial thickness chosen for the virtual image

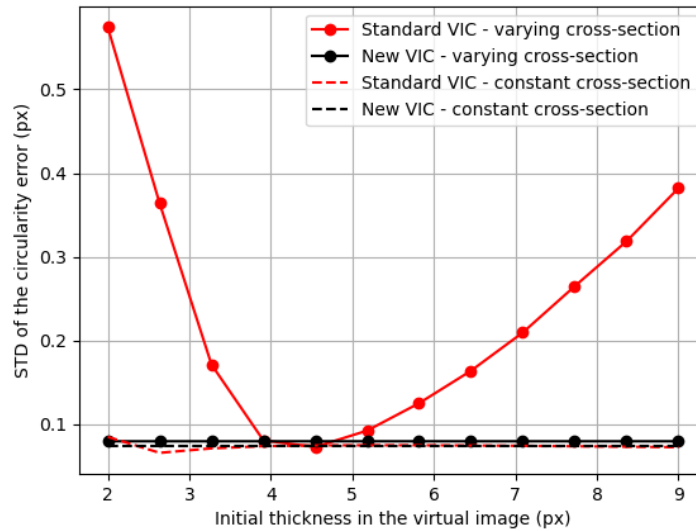


**FIGURE 5** Robustness to initial thickness. Evolution of the circularity error as a function of the initial thickness of the virtual image for classic (red) and proposed (black) VIC solvers; synthetic image of a beam with constant (dashed) and varying (solid) cross-section thickness  $t_v$ .

(which is a classical VIC parameter) can have an influence on the quality of the centerline estimation. This is not the case for a curved beam of constant cross-section, which is the framework for which the standard VIC algorithm was developed<sup>51</sup>. On the other hand, we can notice that the proposed new VIC method does not depend on the initial thickness. This result also

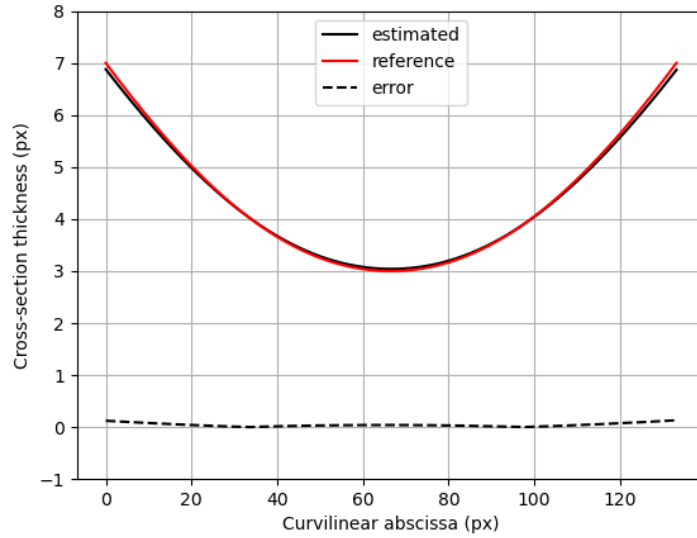


**FIGURE 6** Accuracy of the cross-section thickness estimation  $t_r$  as a function of the curvilinear abscissa. Comparison with the reference value.

seems to confirm that it is important to solve the coupled problem (15) monolithically (*i.e.* by directly solving (15)) rather than sequentially (as imagined in remark 2).

### Cross-section thickness estimation

With such a synthetic example, it is also possible to estimate the accuracy of the determined thickness  $t_r$  from the thickness parameter  $t$ . The evolution of the estimated thickness  $t_r$  is given as a function of the curvilinear abscissa in Fig. 6. It is compared to the reference thickness value prescribed in the construction of the synthetic real image. It can be seen that the proposed VIC method provides, in addition to a subpixel identification of the centerline position, a very good estimate of the thickness and its evolution along the beam. The mean value of the thickness error is around 0.04 pixels in this example. This is an original contribution to the VIC method.

## 5.2 | Synthetic beam lattice

In the next step, we assess the performance of our method to build an accurate and analysis-suitable image-based isogeometric twin of a repetitive lattice microstructure (such as produced with AM). More precisely, the unit cell of an auxetic lattice meta-material is analysed with our VIC approach and then mechanical simulations are performed considering both tension and compression of a unit cell and a full lattice in the large deformation regime. The results for this example regarding VIC are grouped in Fig. 7, while the ones corresponding to the mechanical simulations are presented in Fig. 8.

The auxetic unit cell pattern is taken from<sup>74</sup>. It was obtained using SIMP based topology optimization with a prescribed negative Poisson's ratio under finite deformation. The density pixel map resulting from the topology optimization is used as the reference grayscale image of size  $80 \times 80$  pixel<sup>2</sup>.

### Initialization of the VIC algorithm

Let us first mention that the determination of the beam lattice topology is straightforward in this case since we only need to study one unit cell. A beam model made of 12 quadratic B-spline beams with 4 control points each is used as initial guess, see Fig. 7(a) (top). The initial cross-section thickness is taken constant and equal to 7 pixels. The same discretization is used for the centerline geometry and the cross-section thickness, such that each control point is equipped with 3 DOF. The initial beam model has 108 DOF only. The reference  $f$  and virtual  $g$  images of the long vertical beam on the left are plotted in the parametric space in Fig. 7 (middle). The initial virtual image has a constant thickness and the beam of the real image is not symmetric.



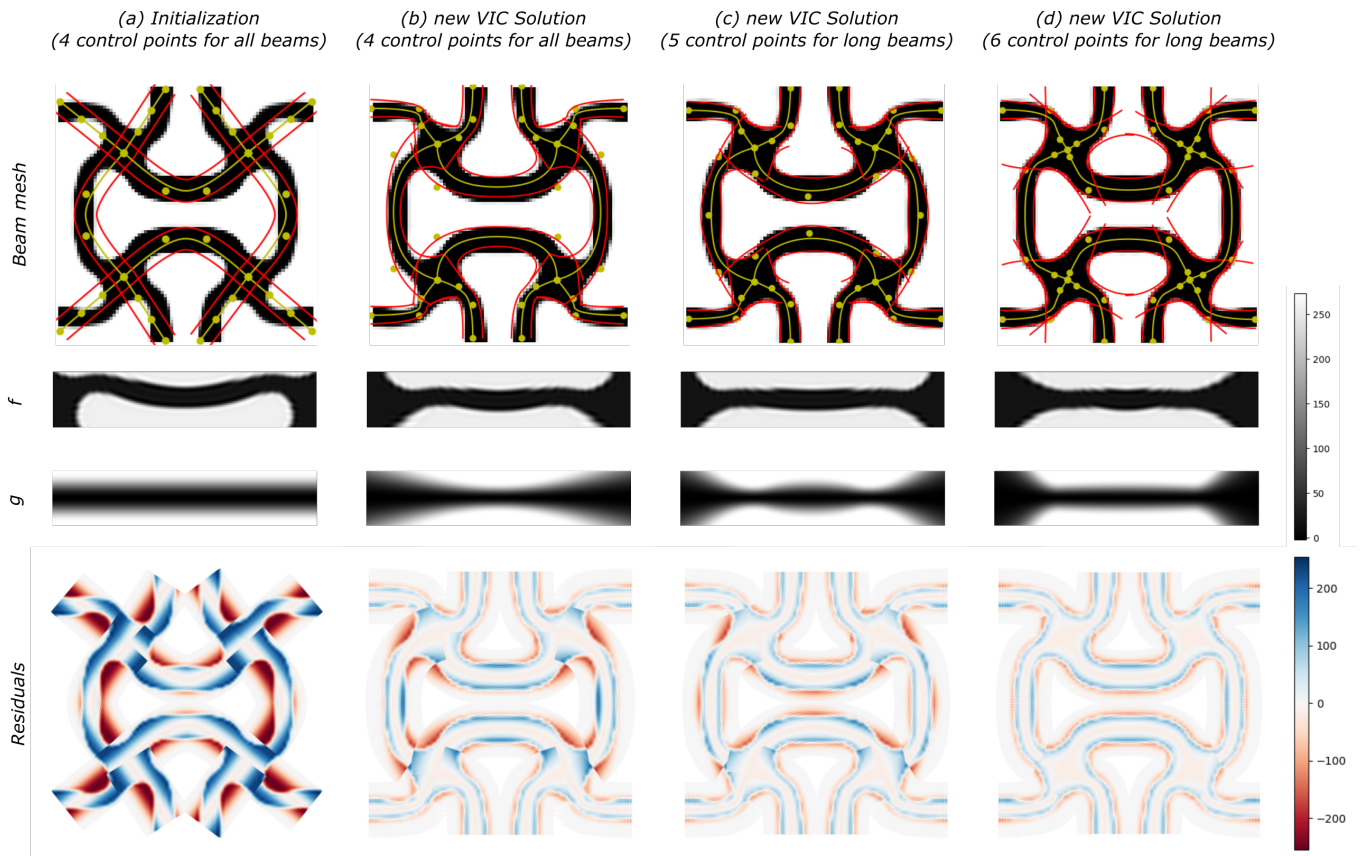


**FIGURE 7** Example of an auxetic lattice pattern. From top to bottom: the beam spline mesh (centerline and associated control points in yellow and beam boundaries due to the thickness in red) superimposed on the image; real image  $f$  interpolated in the parametric space for one arbitrary single beam (left long vertical beam); the corresponding virtual image  $g$ ; the residuals of each beam mapped in the image coordinate system. From left to right: the initialization with 4 control points for each beam; the converged solution using the proposed method with 4, 5 and 6 control points per long beams, respectively.

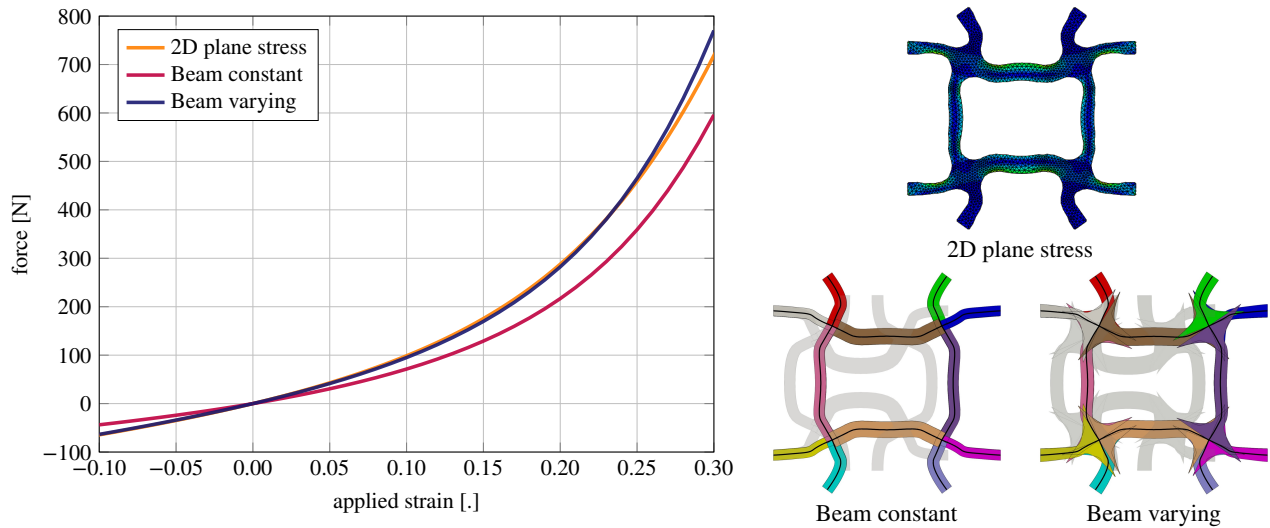
The residual of each beam is mapped in the physical space, see Fig. 7(a) (bottom). One can notice that the residual levels are important, which reflects the coarseness of the initial approximation.

### Results of the proposed VIC strategy

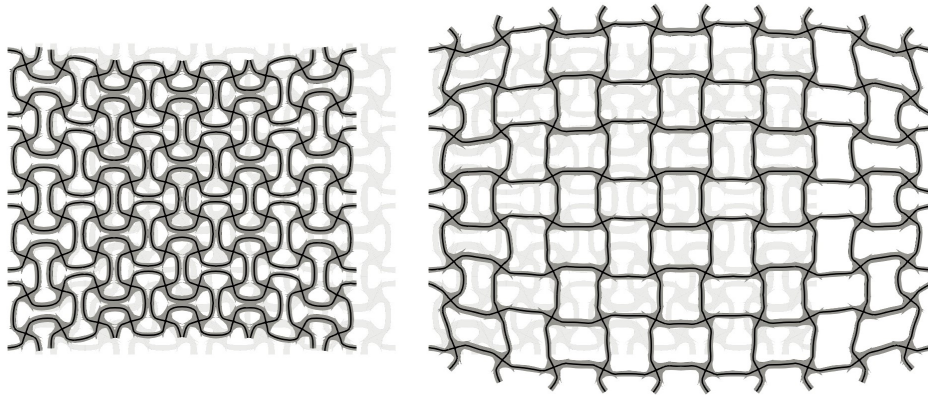
The proposed VIC variant is applied using the aforementioned initialization. As in the previous example, all control points belonging to the image edges are required to remain on the edges. In addition, since the image represents a unit cell that is to be repeated periodically, a  $G^1$  periodicity condition was also prescribed by penalizing the first two layers of control points close to the cell boundary<sup>75</sup>. The associated result is given in Fig. 7(b). The geometry is efficiently optimized but the grayscale residuals seem to show that the thickness approximation subspace is not enough fine, at least for the long beams. This can also be seen when looking at images  $f$  and  $g$ .

### Refinement of the VIC model

Based on this observation, we chose to refine the model by progressively adding knots in the knot vector of the four long beams. Two refined models were considered, a model with one additional control point (120 DOF) and another one with two (132 DOF). The corresponding solutions are given in Figs. 7(c) and (d), respectively. By looking at the residual field, it can be seen that these models progressively improve the representation of the complex geometry and thickness of this unit cell. Quantitatively, the standard deviation of the residual is reduced from 48.43 for the initial model (b), to 40.89 with the first refinement (c) and then to 33.12 graylevels for the most refined model (d). Again, even if the residual in VIC is not supposed to vanish, it can be seen on the residual map that  $g$  much better mimics the real image  $f$  of the unit cell, which confirms the accuracy of our method to represent properly lattice microstructure.



(a) Force-strain curves of a single auxetic unit cell in compression/tension and deformed unit cells at 30% tension



(b) Deformation of lattice with  $5 \times 4$  auxetic cells at  $-10\%$  and  $+30\%$  applied strain (using varying beam model)

**FIGURE 8** Mechanical simulation of the auxetic unit cell and a lattice structure.

### Mechanical simulations

The most accurate beam model with degree 2 and 6 control points for the longer beams, see Fig. 7(d), now serves as a basis for the mechanical analysis using the isogeometric collocation method. To ensure the accuracy of the analysis, the splines bases for the representation of the solution fields, see (29), are  $k$ -refined to degree 6 with 14 control points. For the material parameters, Young's modulus  $E = 1.5$  GPa and Poisson's ratio  $\nu = 0.45$  are assumed, which roughly corresponds to laser sintered nylon (Polyamide 12). To start with, the unit cell is subject to unidirectional compression and tension by constraining all DOFs on the left and right boundaries, but applying a horizontal prescribed deformation on the right. Figure 8a shows the resulting force-strain curves for compression up to  $-10\%$  and tension up to  $30\%$  of the width of the cell, as well as the deformed unit cells at  $30\%$  tension. In addition to the “*beam varying*” model resulting from the proposed VIC, we show the results associated to a “*beam constant*” model and a computationally much more elaborate “*2D plane stress*” FEM model. The *beam constant* model has a non-varying thickness that would correspond to the as-designed thickness, while a sufficiently refined mesh of quadratic triangle elements was generated (using the marching squares algorithm) for the FEM model. As can be seen, the results of the proposed VIC beam model almost perfectly coincide with the 2D FEM, while the model with constant thickness underestimates the stiffness at the intersections and thus results in a softer behavior, see<sup>58</sup>. Finally, to illustrate the applicability of the image-based beam model as an isogeometric twin of a lattice, Fig. 8b shows a structure with  $5 \times 4$  repeated unit cells in compression and tension. Here, the auxetic behavior of the metamaterial can clearly be observed.

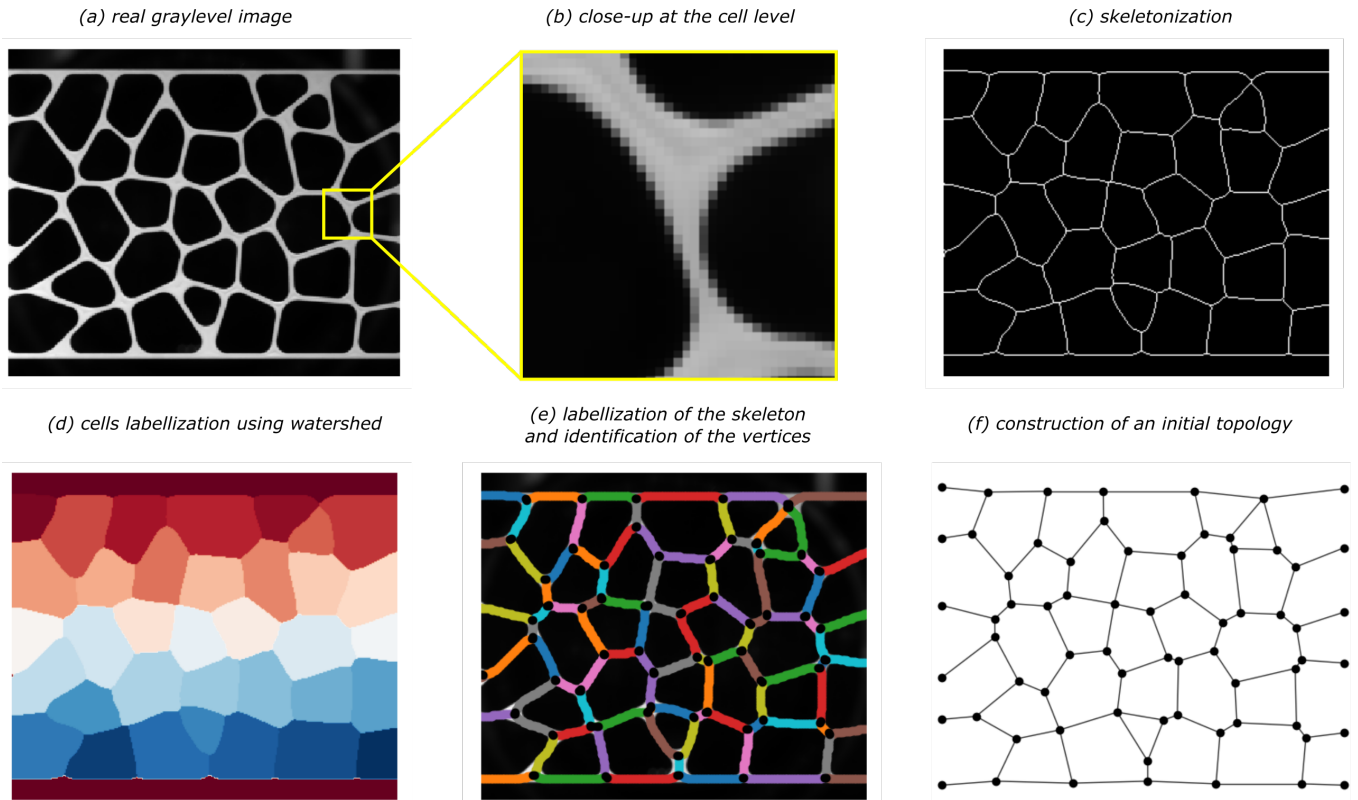


**FIGURE 9** Illustration of the different steps of the proposed generic construction process to obtain the actual topology of a foam-like microstructure from a real graylevel image.

### 5.3 | Real foam-like material

With the last example, we seek to demonstrate the ability of our approach to build an analysis-suitable B-spline beam model from (i) a real image of (ii) a complex random foam-like microstructure, see Figs. 9(a) and (b). Finally, we consider a case where the CAD of the specimen is not known *a priori*. This test case is taken from<sup>76</sup>. The interested reader is referred to the latter contribution for details about the experimental setup.

#### Construction of the topology of the cellular material

With such a complex geometry, the issue of the construction of the topology is a challenge as it cannot reasonably be achieved manually. Here, an automatic procedure has been developed to build a mesh of straight bars (modeling the different struts), starting from the grayscale image of Fig. 9(a). The number of nodes and bars as well as their position are determined automatically by different image analysis techniques. Starting from a binary (thresholding) version of the grayscale image of Fig. 9(a), the proposed procedure consists, in a first step, of performing a skeletonization of the image<sup>44</sup> using the `skeletonize` function (`scikit-image.morphology`)<sup>82</sup>. The latter builds an implicit representation (as a binary image) of the centerlines with a thickness of one pixel, see Fig. 9(c). A levelset image is built from the skeleton using `distance_transform_edt` from `scipy.ndimage`. Then, the cells are labelled using Watershed<sup>46</sup> with the `watershed` function (`scikit-image.segmentation`) using markers defined by the local maximums `peak_local_max` (`scikit-image.feature`) of the levelset image. Each pixel of the image is given an integer value equal to the index of the cell to which it belongs, see Fig. 9(d). Finally, returning to the skeletonized image, each white pixel is given a label that corresponds to the tuple made of the index of the neighboring cells, namely the watershed value of the neighboring pixels. This allows each individual strut to be labelled, see Fig. 9(e) and thus to identify the vertices that have more than two neighbors. Eventually, the nodes are simply connected by straight elements, see Fig. 9(f).

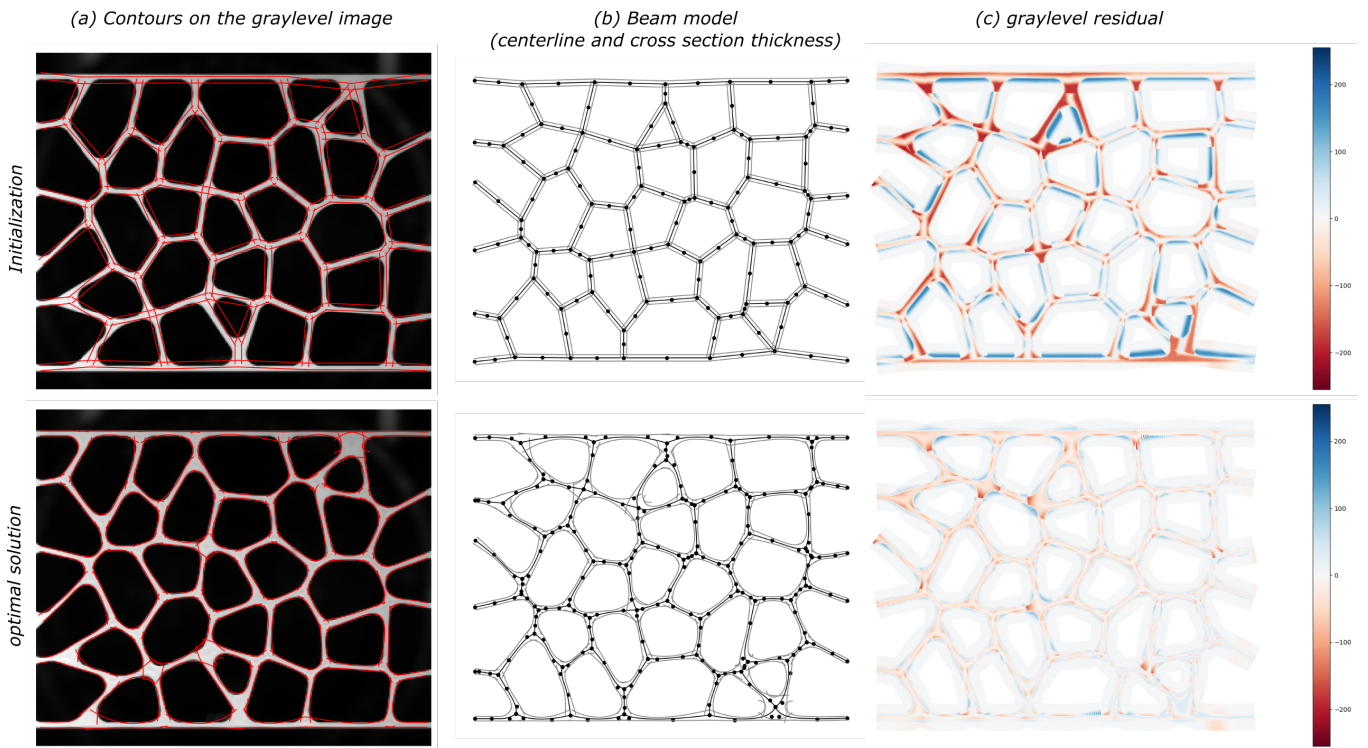


**FIGURE 10** Comparison of the initial (top) and converged (bottom) B-spline beam mesh: (a) plot of the contours of the beam cross-section on the graylevel image, (b) the centerline and control points in black and the beam profiles in gray and (c) the residuals mapped to the physical space.

### Analysis of the proposed VIC results

Even though the positions of the nodes are approximated and the curvature of the beams is neglected when using the above construction process, it provides a very good automatic initialization to the proposed VIC algorithm, as shown in Fig. 10 (top). To run the proposed algorithm, it is also necessary to set the parameters of the virtual image. An arbitrary constant initial thickness of 5 pixels is then assigned to each beam in the model, as depicted in Fig. 10(b) (top). The background (nearly black) and foreground (nearly white) colors are computed from the graylevel values at the nodes. A graylevel gradient can be seen by the naked eye throughout the sample. Anyway, constant values were set for  $g_{bg}$  and  $g_{fg}$  to 7.47 and 172.40, respectively. The standard deviations were equal to 4 and 19.8 graylevels, respectively, which confirms that the foreground color was not homogeneous at all, probably because of inhomogeneous lighting conditions.

As in the previous example, given the morphology of the lattice, and thanks to the B-spline formalism, a refinement by knot-insertion is performed, which results in adding one control point on each beam without changing the geometry. This provides the initialization for a refined model that is optimized by running again the same algorithm. The convergence of the stagnation indicator  $\|\delta\lambda\|/\|\lambda\|$  and standard deviation of the graylevel residual map are plotted in Fig. 11 for the runs before and after refinement. Again, it can be seen that the refinement improves the standard deviation of the graylevel residual from 55.19 with the initial mesh to 26.04 and then to 24.20 graylevels with the refined model. Eventually, by looking at Fig. 10 (bottom), it comes that the optimized B-spline beam model represents the rather complex geometry of the foam-like specimen fairly well. The output is an explicit B-spline representation of the lattice as a light analysis-suitable isogeometric model consisting of 92 beams with 4 control points each and varying thickness.

### Mechanical simulation

For the isogeometric analysis, the solution fields of the beam model with varying thickness are again first refined to degree 6 with 14 control points and the material parameters are chosen as  $E = 1.5$  GPa and  $\nu = 0.45$ . Now, a vertical compression test is simulated by constraining all DOFs at the bottom and top boundaries, but applying a vertical displacement at the top, and constraining only horizontal displacements on the left and right boundaries. Figure 12 shows the resulting force-strain curves for

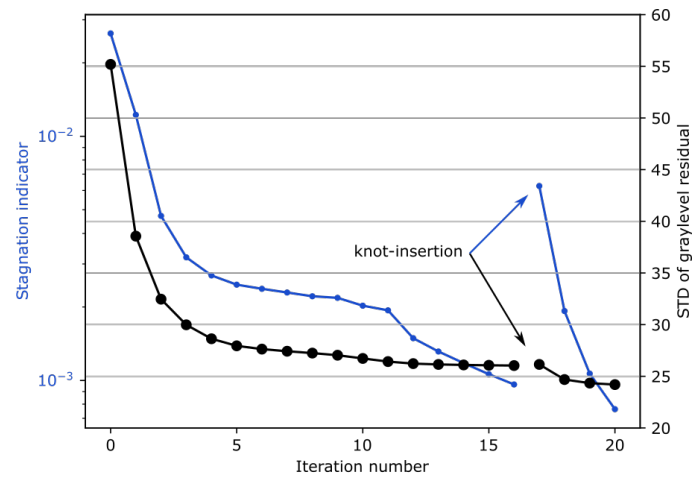


**FIGURE 11** Convergence of the stagnation indicator and the standard deviation of the graylevel residual as a function of the iteration number. Between 16th and 17th iterations, the model was refined by knot-insertion.

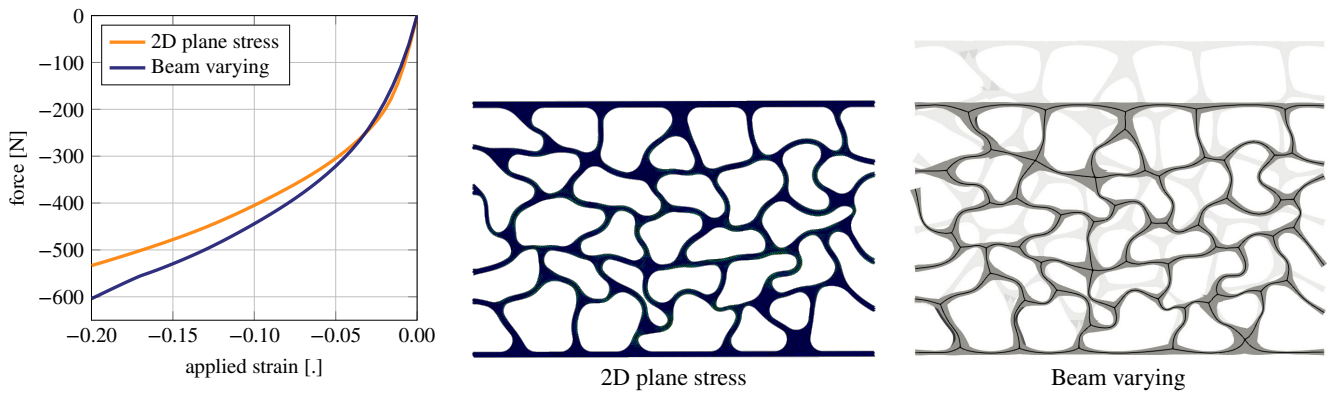


**FIGURE 12** Mechanical simulation of compression of the auxetic foam: force-strain curves and the deformed foam at 20% compression.

compression up to  $-20\%$  of the foam height, as well as the deformed foam at  $-20\%$  compression, again also including the results of a computationally more elaborate 2D plane stress FEM with quadratic triangle elements. As the force-strain curves show, the stiffness of the foam decreases with increasing compression, since struts successively buckle. This can be observed also in the deformed structures visualized in Fig. 12, where the qualitative agreement of the deformation pattern of the image-based isogeometric beam model with varying thickness with the 2D FEM is remarkable. Note that the simulations were terminated here at  $-20\%$  compression right before contacts would occur. It is generally not an issue to consider beam-to-beam contacts in the numerical simulations, see *e.g.*<sup>15</sup> where also inelastic material behavior was included, but here this was avoided for simplicity.

This last test case demonstrates the applicability of our method to obtain an isogeometric beam model, that can serve as an accurate mechanical twin, from real images of a complex and random cellular geometry.

## 6 | CONCLUSION

In this paper, the scope of the Virtual Image Correlation method is extended to low-cost yet predictive image-based models of complex cellular materials such as beam lattices and foams. Several contributions to the method are proposed. First, in addition to the subpixel measurement of the centerline position, it is now possible to precisely estimate the cross-section thickness of the beam. The method is also extended to varying beam cross-sections with estimation of the thickness evolution along the

beam centerline. The method is also successfully extended to complex interconnected beam networks. Finally, techniques are proposed to improve the robustness to initialization. In particular, an automatic construction of an initial topology from images was proposed for a random architecture. The present paper shows, with several examples, that it is possible to build directly from an image a sample-specific digital twin, in the form of an analysis-suitable isogeometric beam model. The comparison with computationally more elaborate solid FEM of image-based models demonstrates that the method can build a model with an extremely low number of degrees of freedom, yet predictive in different loading conditions in the large deformation regime.

Future perspectives concern the extension of the proposed VIC method to 3D from volume images. First, the most delicate issue may concern the initialization of the topology from images (see Fig. 9) if the latter is unknown *a priori* (e.g. random foam). In this case, it will be necessary to develop 3D extensions of the image analysis algorithms used. For deterministic architectures (e.g. lattices), the as-designed geometry can be used as an initial estimate. Another issue concerns the parameterization of the cross-section. Here in 2D, a scalar function of  $\xi$  was sufficient to represent the thickness of the beam. However, in 3D one would have to decide *a priori* on the type of cross-section geometry, *i.e.* a circular or square cross-section could also be parameterized by a scalar radius (or diameter), an ellipse or a rectangle by two parameters, etc. Even further, free-form cross-section geometries could be defined by radial spline parameterizations. Let us notice at this stage that for better efficiency a Domain Decomposition (DD) implementation, where each beam-wise problem is solved in parallel, could be performed, using similar strategies as the ones used for DD-DIC<sup>77,78</sup>. The construction of the initial descriptor could be assisted with artificial intelligence<sup>79</sup>. Another perspective is the use of such a numerical framework for beam-Digital Image Correlation<sup>80,81</sup>, possibly aided by a beam-like mechanical regularization<sup>76</sup>.

## ACKNOWLEDGMENTS

The authors would like to thank Mohammad Shojaee from TU Darmstadt for assistance with the 2D FEM simulations demonstrated in Figs. 8 and 12. O.W. acknowledges financial support of the Deutsche Forschungsgemeinschaft (DFG, German Research Foundation) – grant no. 460684687.

## References

1. M. Benedetti, A. Du Plessis, R. Ritchie, M. Dallago, S. Razavi, F. Berto, Architected cellular materials: A review on their mechanical properties towards fatigue-tolerant design and fabrication, *Materials Science and Engineering: R: Reports* 144 (2021) 100606.
2. T. A. Schaedler, W. B. Carter, Architected cellular materials, *Annual Review of Materials Research* 46 (2016) 187–210.
3. M. F. Ashby, T. Evans, N. A. Fleck, J. Hutchinson, H. Wadley, L. Gibson, *Metal foams: a design guide*, Elsevier (2000).
4. L. J. Gibson, Cellular solids, *MRS Bulletin* 28 (4) (2003) 270–274.
5. A. Somera, M. Poncelet, N. Auffray, J. Réthoré, Quasi-periodic lattices: Pattern matters too, *Scripta Materialia* 209 (2022) 114378.
6. R. Khajehtourian, D. M. Kochmann, Soft adaptive mechanical metamaterials, *Frontiers in Robotics and AI* 8 (2021) 121.
7. S. Babae, J. Shim, J. C. Weaver, E. R. Chen, N. Patel, K. Bertoldi, 3D soft metamaterials with negative Poisson's ratio, *Advanced Materials* 25 (36) (2013) 5044–5049.
8. M. Rashed, M. Ashraf, R. Mines, P. J. Hazell, Metallic microlattice materials: A current state of the art on manufacturing, mechanical properties and applications, *Materials & Design* 95 (2016) 518–533.
9. A. Seharing, A. H. Azman, S. Abdullah, A review on integration of lightweight gradient lattice structures in additive manufacturing parts, *Advances in Mechanical Engineering* 12 (6) (2020) 1687814020916951.
10. L. Ren, Z. Wang, L. Ren, Z. Han, Q. Liu, Z. Song, Graded biological materials and additive manufacturing technologies for producing bioinspired graded materials: An overview, *Composites Part B: Engineering* (2022) 110086.

11. J. U. Surjadi, L. Gao, H. Du, X. Li, X. Xiong, N. X. Fang, Y. Lu, Mechanical metamaterials and their engineering applications, *Advanced Engineering Materials* 21 (3) (2019) 1800864.
12. S. Heinze, T. Bleistein, A. Düster, S. Diebels, A. Jung, Experimental and numerical investigation of single pores for identification of effective metal foams properties (2018).
13. J. R. Greer, V. S. Deshpande, Three-dimensional architected materials and structures: Design, fabrication, and mechanical behavior, *MRS Bulletin* 44 (10) (2019) 750–757 (2019).
14. O. Weeger, N. Boddeti, S.-K. Yeung, S. Kaijima, M. Dunn, Digital Design and Nonlinear Simulation for Additive Manufacturing of Soft Lattice Structures, *Additive Manufacturing* 25 (2019) 39–49 (2019).
15. O. Weeger, I. Valizadeh, Y. Mistry, D. Bhate, Inelastic finite deformation beam modeling, simulation, and validation of additively manufactured lattice structures, *Additive Manufacturing Letters* 4 (2023) 100111.
16. E. Hernández-Nava, C. Smith, F. Derguti, S. Tammam-Williams, F. Léonard, P. J. Withers, I. Todd, R. Goodall, The effect of defects on the mechanical response of Ti-6Al-4V cubic lattice structures fabricated by electron beam melting, *Acta Materialia* 108 (2016) 279–292.
17. M. Dallago, B. Winiarski, F. Zanini, S. Carmignato, M. Benedetti, On the effect of geometrical imperfections and defects on the fatigue strength of cellular lattice structures additively manufactured via selective laser melting, *International Journal of Fatigue* 124 (2019) 348–360.
18. N. Korshunova, I. Papaioannou, S. Kollmannsberger, D. Straub, E. Rank, Uncertainty quantification of microstructure variability and mechanical behavior of additively manufactured lattice structures, *Computer Methods in Applied Mechanics and Engineering* 385 (2021) 114049.
19. A. Almalki, D. Downing, B. Lozanovski, R. Tino, A. Du Plessis, M. Qian, M. Brandt, M. Leary, A Digital-Twin Methodology for the Non-destructive Certification of Lattice Structures, *JOM* 74 (4) (2022) 1784–1797.
20. E. Maire, A. Fazekas, L. Salvo, R. Dendievel, S. Youssef, P. Cloetens, J. M. Letang, X-ray tomography applied to the characterization of cellular materials. related finite element modeling problems, *Composites science and technology* 63 (16) (2003) 2431–2443.
21. A. Düster, H.-G. Sehlhorst, E. Rank, Numerical homogenization of heterogeneous and cellular materials utilizing the finite cell method, *Computational Mechanics* 50 (4) (2012) 413–431.
22. L. Liu, P. Kamm, F. García-Moreno, J. Banhart, D. Pasini, Elastic and failure response of imperfect three-dimensional metallic lattices: the role of geometric defects induced by selective laser melting, *Journal of the Mechanics and Physics of Solids* 107 (2017) 160–184.
23. B. Lozanovski, M. Leary, P. Tran, D. Shidid, M. Qian, P. Choong, M. Brandt, Computational modelling of strut defects in SLM manufactured lattice structures, *Materials & Design* 171 (2019) 107671.
24. N. Korshunova, G. Alaimo, S. Hosseini, M. Carraturo, A. Reali, J. Niiranen, F. Auricchio, E. Rank, S. Kollmannsberger, Bending behavior of octet-truss lattice structures: Modelling options, numerical characterization and experimental validation, *Materials & Design* 205 (2021) 109693.
25. T. J. Hughes, J. A. Cottrell, Y. Bazilevs, Isogeometric analysis: CAD, finite elements, NURBS, exact geometry and mesh refinement, *Computer methods in applied mechanics and engineering* 194 (39-41) (2005) 4135–4195.
26. J. A. Cottrell, T. J. Hughes, Y. Bazilevs, *Isogeometric analysis: toward integration of CAD and FEA*, John Wiley & Sons (2009).
27. J. A. Evans, Y. Bazilevs, I. Babuška, T. J. Hughes, n-Widths, sup-infs, and optimality ratios for the k-version of the isogeometric finite element method, *Computer Methods in Applied Mechanics and Engineering* 198 (21-26) (2009) 1726–1741.

28. W. E. Lorensen, H. E. Cline, Marching cubes: A high resolution 3D surface construction algorithm, *ACM siggraph computer graphics* 21 (4) (1987) 163–169.
29. D. Rajon, W. E. Bolch, Marching cube algorithm: review and trilinear interpolation adaptation for image-based dosimetric models, *Computerized Medical Imaging and Graphics* 27 (5) (2003) 411–435.
30. C. V. Verhoosel, G. Van Zwieten, B. Van Rietbergen, R. de Borst, Image-based goal-oriented adaptive isogeometric analysis with application to the micro-mechanical modeling of trabecular bone, *Computer Methods in Applied Mechanics and Engineering* 284 (2015) 138–164.
31. S. C. Divi, C. V. Verhoosel, F. Auricchio, A. Reali, E. H. van Brummelen, Topology-preserving scan-based immersed isogeometric analysis, *Computer Methods in Applied Mechanics and Engineering* 392 (2022) 114648.
32. D. Schillinger, M. Ruess, The finite cell method: A review in the context of higher-order structural analysis of CAD and image-based geometric models, *Archives of Computational Methods in Engineering* 22 (3) (2015) 391–455.
33. A. Rouwane, R. Bouclier, J.-C. Passieux, J.-N. Périé, Adjusting fictitious domain parameters for fairly priced image-based modeling: Application to the regularization of digital image correlation, *Computer Methods in Applied Mechanics and Engineering* 373 (2021) 113507.
34. G. Legrain, P. Cartraud, I. Perreard, N. Moës, An X-FEM and level set computational approach for image-based modelling: application to homogenization, *International Journal for Numerical Methods in Engineering* 86 (7) (2011) 915–934.
35. J. Wang, G. Zhou, M. Hillman, A. Madra, Y. Bazilevs, J. Du, K. Su, Consistent immersed volumetric Nitsche methods for composite analysis, *Computer Methods in Applied Mechanics and Engineering* 385 (2021) 114042.
36. T. Hoang, C. V. Verhoosel, C.-Z. Qin, F. Auricchio, A. Reali, E. H. van Brummelen, Skeleton-stabilized immersogeometric analysis for incompressible viscous flow problems, *Computer Methods in Applied Mechanics and Engineering* 344 (2019) 421–450.
37. X. Wei, B. Marussig, P. Antolin, A. Buffa, Immersed boundary-conformal isogeometric method for linear elliptic problems, *Computational Mechanics* 68 (6) (2021) 1385–1405.
38. P. Antolin, T. Hirschler, Quadrature-free Immersed Isogeometric Analysis, *Engineering with Computers* 38 (2022) 4475–4499.
39. Y. Zhang, Y. Bazilevs, S. Goswami, C. L. Bajaj, T. J. Hughes, Patient-specific vascular NURBS modeling for isogeometric analysis of blood flow, *Computer methods in applied mechanics and engineering* 196 (29-30) (2007) 2943–2959.
40. B. Urick, T. M. Sanders, S. S. Hossain, Y. J. Zhang, T. J. Hughes, Review of patient-specific vascular modeling: template-based isogeometric framework and the case for CAD, *Archives of Computational Methods in Engineering* 26 (2) (2019) 381–404.
41. Y. Yu, Y. J. Zhang, K. Takizawa, T. E. Tezduyar, T. Sasaki, Anatomically realistic lumen motion representation in patient-specific space–time isogeometric flow analysis of coronary arteries with time-dependent medical-image data, *Computational Mechanics* 65 (2) (2020) 395–404.
42. S. Morganti, F. Auricchio, D. Benson, F. Gambarin, S. Hartmann, T. Hughes, A. Reali, Patient-specific isogeometric structural analysis of aortic valve closure, *Computer methods in applied mechanics and engineering* 284 (2015) 508–520.
43. T. Terahara, K. Takizawa, T. E. Tezduyar, Y. Bazilevs, M.-C. Hsu, Heart valve isogeometric sequentially-coupled FSI analysis with the space–time topology change method, *Computational Mechanics* 65 (4) (2020) 1167–1187.
44. T. Y. Zhang, C. Y. Suen, A fast parallel algorithm for thinning digital patterns, *Communications of the ACM* 27 (3) (1984) 236–239.
45. J.A. Sethian, *Level Set Methods and fast marching methods*, Cambridge University Press (1996).



46. S. Beucher, C. Lantuéjoul, Use of watersheds in contour detection, in: International Workshop on image processing: Real-time Edge and Motion detection/estimation, Rennes, France (1979).
47. Y. Sun, J. H. Pang, C. K. Wong, F. Su, Finite element formulation for a digital image correlation method, *Applied optics* 44 (34) (2005) 7357–7363.
48. F. Hild, S. Roux, Digital image correlation: from displacement measurement to identification of elastic properties—a review, *Strain* 42 (2) (2006) 69–80.
49. J. Neggers, B. Blaysat, J. P. Hoefnagels, M. G. Geers, On image gradients in digital image correlation, *International Journal for Numerical Methods in Engineering* 105 (4) (2016) 243–260.
50. J.-C. Passieux, R. Bouclier, Classic and inverse compositional gauss-newton in global DIC, *International Journal for Numerical Methods in Engineering* 119 (6) (2019) 453–468.
51. M. L. François, B. Semin, H. Auradou, Identification of the shape of curvilinear beams and fibers, in: *Applied Mechanics and materials*, Vol. 24, Trans Tech Publ (2010) 359–364.
52. B. Semin, H. Auradou, M. L. François, Accurate measurement of curvilinear shapes by virtual image correlation, *The European Physical Journal-Applied Physics* 56 (1) (2011).
53. J. Réthoré, M. François, Curve and boundaries measurement using B-splines and virtual images, *Optics and Lasers in Engineering* 52 (0) (2014) 145–155.
54. M. L. M. François, A. Bloch, J.-C. Thomas, Metrology of contours by the virtual image correlation technique, in: *Advancement of Optical Methods in Experimental Mechanics*, Vol. 3, Springer (2016) 239–246.
55. Z. Jiang, O. Mayeur, J.-F. Witz, P. Lecomte-Grosbras, J. Dequidt, M. Cosson, C. Duriez, M. Brieu, Virtual image correlation of magnetic resonance images for 3D geometric modelling of pelvic organs, *Strain* 55 (3) (2019) e12305.
56. M. Baconnais, J. Réthoré, M. François, Improvement of the digital image correlation close to the borders of an object, *Strain* 56 (3) (2020) e12340.
57. M. François, Uncertainty of the virtual image correlation method, *International Journal for Numerical Methods in Engineering* 123 (18) (2022) 4367–4390.
58. O. Weeger, S.-K. Yeung, M. Dunn, Isogeometric collocation methods for Cosserat rods and rod structures, *Computer Methods in Applied Mechanics and Engineering* 316 (2017) 100–122.
59. O. Weeger, S.-K. Yeung, M. L. Dunn, Fully isogeometric modeling and analysis of nonlinear 3D beams with spatially varying geometric and material parameters, *Computer Methods in Applied Mechanics and Engineering* 342 (2018) 95–115.
60. O. Weeger, Isogeometric sizing and shape optimization of 3d beams and lattice structures at large deformations, *Structural and Multidisciplinary Optimization* 65 (2) (2022) 1–22.
61. E. Jones, T. Oliphant, P. Peterson, et al., *Scipy: Open source scientific tools for Python* (2001).
62. J. Réthoré, S. Roux, F. Hild, An extended and integrated digital image correlation technique applied to the analysis of fractured samples: The equilibrium gap method as a mechanical filter, *European Journal of Computational Mechanics/Revue Européenne de Mécanique Numérique* 18 (3-4) (2009) 285–306.
63. J. Kiendl, R. Schmidt, R. Wüchner, K.-U. Bletzinger, Isogeometric shape optimization of shells using semi-analytical sensitivity analysis and sensitivity weighting, *Computer Methods in Applied Mechanics and Engineering* 274 (2014) 148–167.
64. R. Bouclier, T. Hirschler, *IGA: Non-conforming Coupling and Shape Optimization of Complex Multipatch Structures*, John Wiley & Sons (2022).

65. M. Chapelier, R. Bouclier, J.-C. Passieux, Free-form deformation digital image correlation (ffd-dic): a non-invasive spline regularization for arbitrary finite element measurements, *Computer Methods in Applied Mechanics and Engineering* 384 (2021) 113992.
66. G. Colantonio, M. Chapelier, R. Bouclier, J.-C. Passieux, E. Mareníć, Noninvasive multilevel geometric regularization of mesh-based three-dimensional shape measurement, *International Journal for Numerical Methods in Engineering* 121 (9) (2020) 1877–1897.
67. L. Piegl, W. Tiller, *The NURBS book*, Springer Science & Business Media (1996).
68. J. A. Cottrell, T. J. Hughes, Y. Bazilevs, *Isogeometric analysis: toward integration of CAD and FEA*, John Wiley & Sons (2009).
69. O. Weeger, D. Schillinger, R. Müller, Mixed isogeometric collocation for geometrically exact 3D beams with elasto-viscoplastic material behavior and softening effects, *Computer Methods in Applied Mechanics and Engineering* 399 (2022) 115456.
70. D. Vo, P. Nanakorn, A total Lagrangian Timoshenko beam formulation for geometrically nonlinear isogeometric analysis of planar curved beams, *Acta Mechanica* 231 (7) (2020) 2827–2847.
71. F. Auricchio, L. Beirão da Veiga, T. Hughes, A. Reali, G. Sangalli, *Isogeometric Collocation Methods*, *Mathematical Models and Methods in Applied Sciences* 20 (11) (2010) 2075–2107.
72. F. Auricchio, L. Beirão da Veiga, J. Kiendl, C. Lovadina, A. Reali, Locking-free isogeometric collocation methods for spatial Timoshenko rods, *Computer Methods in Applied Mechanics and Engineering* 263 (2013) 113–126.
73. J. Cottrell, T. Hughes, A. Reali, Studies of refinement and continuity in isogeometric structural analysis, *Computer methods in applied mechanics and engineering* 196 (41-44) (2007) 4160–4183.
74. F. Wang, O. Sigmund, J. Jensen, Design of materials with prescribed nonlinear properties, *Journal of the Mechanics and Physics of Solids* 69 (2014) 156–174.
75. J. Kiendl, K.-U. Bletzinger, J. Linhard, R. Wüchner, Isogeometric shell analysis with Kirchhoff–Love elements, *Computer methods in applied mechanics and engineering* 198 (49-52) (2009) 3902–3914.
76. A. Rouwane, R. Bouclier, J.-C. Passieux, J.-N. Périé, Architecture-Driven Digital Image Correlation Technique (ADDICT) for the measurement of sub-cellular kinematic fields in speckle-free cellular materials, *International Journal of Solids and Structures* 234-235 (2022) 111223.
77. J.-C. Passieux, J.-N. Périé, M. Salaün, A dual domain decomposition method for finite element digital image correlation, *International Journal for Numerical Methods in Engineering* 102 (10) (2015) 1670–1682.
78. R. Bouclier, J.-C. Passieux, A domain coupling method for finite element digital image correlation with mechanical regularization: Application to multiscale measurements and parallel computing, *International Journal for Numerical Methods in Engineering* 111 (2) (2017) 123–143.
79. H. Ahmadian, P. Mageswaran, B. A. Walter, D. M. Blakaj, E. C. Bourekas, E. Mendel, W. S. Marras, S. Soghrati, Toward an artificial intelligence-assisted framework for reconstructing the digital twin of vertebra and predicting its fracture response, *International Journal for Numerical Methods in Biomedical Engineering* 38 (6) (2022) e3601.
80. J. Réthoré, T. Elguedj, P. Simon, M. Coret, On the Use of NURBS Functions for Displacement Derivatives Measurement by Digital Image Correlation, *Experimental Mechanics* 50 (7) (2010) 1099–1116.
81. F. Hild, S. Roux, R. Gras, N. Guerrero, M. E. Marante, J. Flórez-López, Displacement measurement technique for beam kinematics, *Optics and Lasers in Engineering* 47 (3) (2009) 495–503.
82. S. Van der Walt, J. Schönberger, J. Nunez-Iglesias, F. Boulogne, J. Warner, N. Yager, E. Gouillart, T. Yu, scikit-image: image processing in Python, *PeerJ* 2 (2014) e453.

**How to cite this article:** J.-C. Passieux, R. Bouclier, and O. Weeger (2022), Virtual image correlation for beams with varying cross-sections for image-based isogeometric twins of lattice structures, *Int. J. Numer. Meth. Engrg.*, .